

DualDynamics: Synergizing Implicit and Explicit Methods for Robust Irregular Time Series Analysis

YongKyung Oh^{1*}, Dong-Young Lim^{2,3*}, & Sungil Kim^{2,3†}

¹Medical & Imaging Informatics (MII) Group, University of California, Los Angeles (UCLA)

²Department of Industrial Engineering, Ulsan National Institute of Science and Technology (UNIST)

³Artificial Intelligence Graduate School, Ulsan National Institute of Science and Technology (UNIST)
yongkyungh@mednet.ucla.edu, {dlim, sungil.kim}@unist.ac.kr

Abstract

Real-world time series analysis faces significant challenges when dealing with irregular and incomplete data. While Neural Differential Equation (NDE) based methods have shown promise, they struggle with limited expressiveness, scalability issues, and stability concerns. Conversely, Neural Flows offer stability but falter with irregular data. We introduce **DualDynamics**, a novel framework that synergistically combines NDE-based method and Neural Flow-based method. This approach enhances expressive power while balancing computational demands, addressing critical limitations of existing techniques. We demonstrate DualDynamics' effectiveness across diverse tasks: classification of robustness to dataset shift, irregularly-sampled series analysis, interpolation of missing data, and forecasting with partial observations. Our results show consistent outperformance over state-of-the-art methods, indicating DualDynamics' potential to advance irregular time series analysis significantly.

Introduction

Effectively modeling time series data is a cornerstone in machine learning, supporting numerous applications across diverse sectors. This significance has driven substantial research endeavors aimed at developing novel methodologies capable of accurately capturing the complexities of continuous latent processes (Chen et al. 2018; Kidger et al. 2020; Oh, Lim, and Kim 2024).

Recent advancements in this field have led to two distinct approaches: implicit methods, such as Neural Differential Equation (NDE)-based techniques, and explicit methods, exemplified by Neural Flows. Neural Ordinary Differential Equations (Neural ODEs) (Chen et al. 2018), Neural Controlled Differential Equations (Neural CDEs) (Kidger et al. 2020) and Neural Stochastic Differential Equations (Neural SDEs) (Oh, Lim, and Kim 2024) have emerged as prominent implicit meth-

ods, recognized for their ability to learn continuous-time dynamics and underlying temporal structures. These approaches directly learn continuous latent representations based on vector fields parameterized by neural networks. However, NDE-based methods face challenges including limited expressive power (Dupont, Doucet, and Teh 2019; Massaroli et al. 2020b; Chalvidal et al. 2021; Kidger 2022) and scalability issues when analyzing irregular or complex time series data (Norcliffe et al. 2020; Morrill et al. 2021, 2022; Irie, Faccio, and Schmidhuber 2022; Pal et al. 2023). These limitations are attributed to data complexity, sequence length variations, and the stability constraints of numerical solvers (He and Semnani 2023; Westny et al. 2023).

In parallel, explicit methods such as Neural Flows have been developed, focusing on directly mapping solution curves using neural networks (Lu et al. 2018; Sonoda and Murata 2019; Massaroli et al. 2020a; Biloš et al. 2021). These approaches offer invertible solutions and enhanced stability through the change of variables formula (Kobyzev, Prince, and Brubaker 2020; Papamakarios et al. 2021). However, they struggle with irregularly-sampled time series and are sensitive to initial state and corresponding initial value problem.

To address the limitations of both implicit and explicit methods, we introduce **DualDynamics**, a novel framework that synergistically combines NDE-based model and Neural Flow-based model. This approach aims to leverage the strengths of both paradigms: the flexibility of implicit methods in handling irregular data and the stability and computational efficiency of explicit methods. By integrating these complementary approaches, DualDynamics seeks to enhance expressive power, improve scalability, and maintain stability in modeling complex, irregular time series data.

Related Works

The landscape of neural differential equations for time series modeling has been dominated by two distinct approaches: implicit methods, exemplified by Neural ODEs, Neural CDEs and Neural SDEs, and explicit methods, such as Neural Flows. These approaches fundamentally differ in how they represent and solve the

*These two authors are equal contributors to this work and designated as co-first authors.

†Corresponding Author

Copyright © 2025, Association for the Advancement of Artificial Intelligence (www.aaai.org). All rights reserved.

underlying dynamics of time-evolving systems.

Implicit methods for continuous dynamics

Implicit methods in deep learning for time series modeling solve differential equations numerically, allowing for adaptive computation and flexible handling of irregular data. These methods have gained significant attention due to their ability to model complex dynamics.

Let $\mathbf{x} = (x_0, x_1, \dots, x_n)$ be a vector of original irregularly-sampled observations and $\mathbf{z}(t)$ denote a latent state at time t . Continuous latent dynamics $\mathbf{z}(t)$ can be achieved by integration of $d\mathbf{z}(t)$ over time in $[0, t]$. Neural Differential Equations can be expressed as:

$$\text{Neural ODEs: } d\mathbf{z}(t) = f(s, \mathbf{z}(s); \theta_f) ds \quad (1)$$

$$\text{Neural CDEs: } d\mathbf{z}(t) = f(s, \mathbf{z}(s); \theta_f) dX(s) \quad (2)$$

$$\text{Neural SDEs: } d\mathbf{z}(t) = f(s, \mathbf{z}(s); \theta_f) ds + g(s, \mathbf{z}(s); \theta_g) dW(s) \quad (3)$$

with initial condition $\mathbf{z}(0) = h(\mathbf{x}; \theta_h)$, where $h: \mathbb{R}^{d_x} \rightarrow \mathbb{R}^{d_z}$ is an affine function. f and g are neural networks parameterized by θ_f and θ_g , respectively. $X(t)$ is a controlled path for Neural CDEs, and $W(t)$ is a Wiener process for Neural SDEs.

Neural ODEs (Chen et al. 2018) model deterministic dynamics but may struggle with expressiveness and stability for complex trajectories (Dupont, Doucet, and Teh 2019; Massaroli et al. 2020b). Furthermore, Neural CDEs (Kidger et al. 2020) handle irregular time series effectively but can be computationally intensive for long sequences (Morrill et al. 2021). Therefore, recent works introduced extended architecture using Neural CDE. On the other hand, Neural SDEs (Li et al. 2020) incorporate uncertainty modeling but face challenges in training and inference due to their stochastic nature (Jia and Benson 2019; Oh, Lim, and Kim 2024). These methods offer varying approaches to modeling continuous-time dynamics in time series data, each with its own strengths and limitations in handling complexity, irregularity, and uncertainty.

Explicit methods for continuous dynamics

Explicit methods directly model the solution of differential equations, often providing faster computation and improved stability, albeit potentially at the cost of some flexibility. Neural Flows, introduced by Biloš et al. (2021), present a novel approach to directly model the trajectory of the latent state $\mathbf{z}(t)$, in contrast to Neural ODEs which represent the rate of change of $\mathbf{z}(t)$ over time in an integration form. Specifically, $\mathbf{z}(t)$ is expressed as:

$$\mathbf{z}(t) = \mathcal{F}(t, \mathbf{z}(0); \theta_{\mathcal{F}}), \quad (4)$$

with the initial value $\mathbf{z}(0) = h(\mathbf{x}; \theta_h)$, where \mathcal{F} is a neural network parameterized by $\theta_{\mathcal{F}}$. Note that while \mathcal{F} represents the solution to the initial value problem of Neural ODEs, as described in Eq. (1), the formulation of Neural Flows in Eq. (4) does not require the use of an

ODE solver. However, the requirement for the Neural Flow $\mathcal{F}(\cdot, \mathbf{z}(0))$ to be invertible restricts the type of neural network architectures, which may not be suitable if the initial value is unknown or unstable to estimate. In practice, determining the exact flow is challenging since many real-world problems do not have analytical solutions, which can lead to training instability.

Methodology

Model architecture

To illustrate our DualDynamics framework, we utilize Neural CDEs as the primary example in this section. Neural CDEs serve as an effective representation of the implicit component in our dual approach, offering a robust foundation for modeling irregular time series data. Figure 1 shows the conceptual overview of the proposed architecture using Neural CDE (implicit) and Flow-based model (explicit) for classification task.

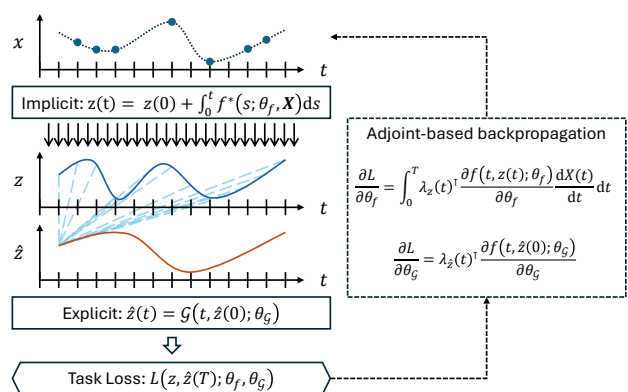


Figure 1: Overview of the proposed DualDynamics

The proposed method combines the stability of flow models with NDE-based model to achieve a better representation of the irregular time series. The flow model, known for its capability to smoothly transform complex distributions, offers inherent stability when dealing with time-varying dynamics. To achieve stability in the latent representation $\mathbf{z}(t)$, we introduce a secondary latent space, denoted by $\hat{\mathbf{z}}(t)$. This secondary latent space is inspired by the principles of Neural Flow and is designed to produce a regularized representation of the original latent variable. From Eq. (2), the latent representation $\mathbf{z}(t)$ can be derived from an initial vector $\mathbf{z}(0)$, which is transformed from the raw input x_0 . Thus, the proposed dual latent variable evolves in time as:

$$\mathbf{z}(t) = \mathbf{z}(0) + \int_0^t f(s, \mathbf{z}(s); \theta_f) dX(s), \quad (5)$$

where the initial value of the first latent representation $\mathbf{z}(0) = h(x_0; \theta_h)$, and $h: \mathbb{R}^{d_x} \rightarrow \mathbb{R}^{d_z}$. As stated in Chen et al. (2018) and Kidger et al. (2020), we focus on the time-evolving state \mathbf{z} from the linear mapping from \mathbf{x}

using h . Eq. (5) can be rewritten as follows:

$$\mathbf{z}(t) = \mathbf{z}(0) + \int_0^t f^*(s; \theta_f, X) ds, \quad (6)$$

where $f^*(s; \theta_f, X) := f(s, \mathbf{z}(s); \theta_f) \frac{dX(s)}{ds}$. Recall that X is generated from \mathbf{x} . Here, we implement X for ‘Hermite Cubic splines with a backward difference’, which is smooth and unique (Morrill et al. 2022). Through this part, we find $\mathbf{z} \in \mathbb{R}^{d_z}$, and then plug it into the following flow model \mathcal{G} as:

$$\hat{\mathbf{z}}(t) = \mathcal{G}(t, \hat{\mathbf{z}}(0); \theta_{\mathcal{G}}), \quad (7)$$

with $\hat{\mathbf{z}}(0) = k(\mathbf{z}; \theta_k)$, and $k : \mathbb{R}^{d_z \times T} \rightarrow \mathbb{R}^{d_z}$. In other words, $\hat{\mathbf{z}}(0)$ is determined by $\mathbf{z}(t)$ for $t \in [0, T]$.

Here, \mathcal{G} satisfies the ODE defined in Eq. (6), i.e., $\frac{d\mathcal{G}(t, \hat{\mathbf{z}}(0))}{dt} = f^*(t; \theta_f, X)$ and $\mathcal{G}(\cdot, \hat{\mathbf{z}}(0))$ is invertible. In summary, after obtaining the primary latent space $\mathbf{z}(t)$, we compute \mathcal{G} with the initial value $\hat{\mathbf{z}}(0)$. This model generates the secondary latent state $\hat{\mathbf{z}}(t)$ without the need to directly determine its derivative $\frac{d\hat{\mathbf{z}}(t)}{dt}$.

Expressive power of flow model \mathcal{G} Flow-based model, which is invertible and differentiable (known as ‘diffeomorphisms’), has the capability of representing any distribution. Given the Neural Flow \mathcal{G} , there exists a unique input $\hat{\mathbf{z}}(0)$ such that, $\hat{\mathbf{z}}(0) = \mathcal{G}^{-1}(t, \hat{\mathbf{z}}(t); \theta_{\mathcal{G}})$. This invertibility ensures a one-to-one mapping between the initial and transformed states, preserving information content. The change of variables formula for probability densities leads to:

$$p_{\mathbf{z}(t)}(\hat{\mathbf{z}}(t)) = p_{\hat{\mathbf{z}}(0)}(\hat{\mathbf{z}}(0)) |\det \mathbf{J}_{\mathcal{G}}(\hat{\mathbf{z}}(0))|^{-1}, \quad (8)$$

where $\mathbf{J}_{\mathcal{G}}(\hat{\mathbf{z}}(0))$ is the Jacobian matrix of \mathcal{G} at $\hat{\mathbf{z}}(0)$, and $|\det \mathbf{J}_{\mathcal{G}}(\hat{\mathbf{z}}(0))|$ is its determinant.

Suppose $\hat{\mathbf{z}}(0) \sim \mathcal{U}([0, 1]^{d_z})$, meaning each component of $\hat{\mathbf{z}}(0)$ is uniformly distributed between 0 and 1. The probability density function of $\hat{\mathbf{z}}(0)$ in this multi-dimensional space is constant, $p_{\hat{\mathbf{z}}(0)}(y) = 1$ if $y \in [0, 1]^{d_z}$. Then, Eq. (8) can be simplified to:

$$p_{\mathbf{z}(t)}(\hat{\mathbf{z}}(t)) = |\det \mathbf{J}_{\mathcal{G}}(\hat{\mathbf{z}}(0))|^{-1}. \quad (9)$$

The determinant of the Jacobian $|\det \mathbf{J}_{\mathcal{G}}(\hat{\mathbf{z}}(0))|$ accounts for the ‘stretching’ or ‘squeezing’ of the volume elements during the transformation. By adjusting $\theta_{\mathcal{G}}$, the model can control how much each part of the space $[0, 1]^{d_z}$ expands, contracts or projects, allowing \mathcal{G} to mold the uniform distribution into any desired complex distribution $p_{\mathbf{z}(t)}$.

Properties of the proposed method

Preservation of probability density It is crucial for ensuring that the total probability across transformations remains constant, enabling accurate modeling of dynamic systems’ evolution without loss or gain of information (Li and Chen 2008; Dinh, Sohl-Dickstein, and Bengio 2016). For each fixed t , $p_{\mathbf{z}(t)}$ and $p_{\hat{\mathbf{z}}(t)}$ be

the probability density functions of $\mathbf{z}(t)$ and $\hat{\mathbf{z}}(t)$, respectively. From the *instantaneous change of variables formula* (Chen et al. 2018), we observe that

$$\frac{\partial \log p_{\mathbf{z}(t)}(\mathbf{z}(t))}{\partial t} = -\text{Tr}(\mathbf{J}_{f^*}(\mathbf{z}(t))), \quad (10)$$

$$\frac{\partial \log p_{\hat{\mathbf{z}}(t)}(\hat{\mathbf{z}}(t))}{\partial t} = -\text{Tr}\left(\mathbf{J}_{\frac{d\mathcal{G}}{dt}}(\hat{\mathbf{z}}(t))\right), \quad (11)$$

where $\text{Tr}(A)$ is the trace of matrix A and \mathbf{J}_{f^*} is the Jacobian matrix of f^* . $\mathbf{J}_{\frac{d\mathcal{G}}{dt}}$ is the Jacobian matrix of $\frac{d\mathcal{G}}{dt}$ and we have used $\frac{d\mathcal{G}(t, \hat{\mathbf{z}}(0))}{dt} = f^*(t; \theta_f, X)$ for all t . Therefore, the total changes in log-density for \mathbf{z} and $\hat{\mathbf{z}}$ from time 0 to t are given by:

$$\begin{aligned} & \log p_{\mathbf{z}(t)}(\mathbf{z}(t)) - \log p_{\mathbf{z}(0)}(\mathbf{z}(0)) \\ &= -\int_0^t \text{Tr}(\mathbf{J}_{f^*}(\mathbf{z}(s))) ds, \end{aligned} \quad (12)$$

$$\begin{aligned} & \log p_{\hat{\mathbf{z}}(t)}(\hat{\mathbf{z}}(t)) - \log p_{\hat{\mathbf{z}}(0)}(\hat{\mathbf{z}}(0)) \\ &= -\int_0^t \text{Tr}\left(\mathbf{J}_{\frac{d\mathcal{G}}{ds}}(\hat{\mathbf{z}}(s))\right) ds, \end{aligned} \quad (13)$$

$$= -\int_0^t \text{Tr}(\mathbf{J}_{f^*}(\hat{\mathbf{z}}(s))) ds, \quad (14)$$

Eq. (12) and Eq. (14) imply that the probability content of corresponding regions in the primary latent space \mathbf{z} and the second latent space $\hat{\mathbf{z}}$ must be the same when the Neural Flow \mathcal{G} is perfectly estimated (Kingma and Dhariwal 2018; Onken et al. 2021).

Computational advantage of flow model \mathcal{G} We are interested in computing the trace of $\mathbf{J}_{\frac{d\mathcal{G}}{ds}}$ in Eq. (13), which is a key quantity to understand the change in log-density. We use Hutchinson’s trace estimator¹ (Hutchinson 1989) used to estimate the trace of a matrix efficiently, especially in situations where the matrix is large and computing the trace directly is computationally expensive² (Adams et al. 2018; Han, Malioutov, and Shin 2015; Grathwohl et al. 2018).

Applying Hutchinson’s trace estimator to $\mathbf{J}_{\frac{d\mathcal{G}}{ds}}$, we have:

$$\text{Tr}\left(\mathbf{J}_{\frac{d\mathcal{G}}{ds}}(\hat{\mathbf{z}}(t))\right) \approx \mathbb{E}_{\mathbf{v}}\left[\mathbf{v}^\top \mathbf{J}_{\frac{d\mathcal{G}}{ds}}(\hat{\mathbf{z}}(t)) \mathbf{v}\right]. \quad (15)$$

Then, Eq. (13) can be rewritten as follows:

$$\begin{aligned} & \log p_{\hat{\mathbf{z}}(t)}(\hat{\mathbf{z}}(t)) - \log p_{\hat{\mathbf{z}}(0)}(\hat{\mathbf{z}}(0)) \\ & \approx -\mathbb{E}_{\mathbf{v}}\left[\int_0^t \mathbf{v}^\top \mathbf{J}_{\frac{d\mathcal{G}}{ds}}(\hat{\mathbf{z}}(s)) \mathbf{v} ds\right] \\ & = -\mathbb{E}_{\mathbf{v}}\left[\int_0^t \mathbf{v}^\top \frac{\partial \mathbf{J}_{\mathcal{G}}(\hat{\mathbf{z}}(s))}{\partial t} \mathbf{v} ds\right]. \end{aligned} \quad (16)$$

¹Hutchinson’s trace estimator states that for a square matrix A , the trace of A can be estimated as: $\text{Tr}(A) \approx \mathbb{E}_{\mathbf{v}}[\mathbf{v}^\top A \mathbf{v}]$, where \mathbf{v} is a random vector with each element drawn independently from a distribution with zero mean and unit variance.

²Hutchinson’s trace estimator significantly reduces computational complexity from $\mathcal{O}(d_z^2)$ for direct trace computation to $\mathcal{O}(d_z)$ for matrix-vector multiplications.

where the last inequality is obtained by changing the order of partial derivatives. Incorporating the flow model \mathcal{G} into the original NDE-based model enhances its expressive power without significantly increasing the computational burden, as opposed to the addition of an extra ODE/CDE formulation.

Parameter optimization

To optimize parameters involved in the proposed method, we employ adjoint-based backpropagation (Chen et al. 2018; Kidger et al. 2020; Kidger 2022). This method allows for efficient gradient computation, ensuring that the information from one step influences and refines the subsequent step, leading to a more unified optimization process. The adjoint method is a powerful technique often used to calculate the gradients of systems governed by differential equations. The basic idea is to recast the derivative computation problem as the adjoint equation (Pontryagin 2018; Pollini, Lavan, and Amir 2018).

Consider an objective function $\mathcal{L}(z, \hat{z}(T); \theta_f, \theta_G)$ that depends on the final value of the second latent state, $\hat{z}(T)$. Then, one can define the adjoint state $\lambda_z(t)$ and $\lambda_{\hat{z}}(t)$ as the gradient of the loss function with respect to the state $z(t)$ and $\hat{z}(t)$:

$$\lambda_z(t) = \frac{\partial \mathcal{L}}{\partial z(t)}, \quad \lambda_{\hat{z}}(t) = \frac{\partial \mathcal{L}}{\partial \hat{z}(t)}. \quad (17)$$

To estimate the model parameters θ_f and θ_G , we compute the gradients of the loss function with respect to these parameters:

$$\frac{\partial \mathcal{L}}{\partial \theta_f} = \int_0^T \lambda_z(t)^\top \frac{\partial f(t, z(t); \theta_f)}{\partial \theta_f} \frac{dX(t)}{dt} dt, \quad (18)$$

$$\frac{\partial \mathcal{L}}{\partial \theta_G} = \lambda_{\hat{z}}(T)^\top \frac{\partial \mathcal{G}(T, \hat{z}(0); \theta_G)}{\partial \theta_G}. \quad (19)$$

Note that $\lambda_z(t)$ can be derived by integration of adjoint dynamics backward in time from T to 0, which is the continuous-time analog to the backpropagation algorithm (Rumelhart, Hinton, and Williams 1986; Kidger, Chen, and Lyons 2021). On the other hand, $\lambda_{\hat{z}}(t)$ is derived by backpropagation algorithm directly.

The DualDynamics framework integrates implicit and explicit components into a unified architecture, enabling concurrent optimization of both elements. This joint learning process ensures that the implicit Neural Differential Equation and the explicit Neural Flow components evolve synergistically, rather than sequentially, thereby capitalizing on their complementary strengths in a single, cohesive optimization procedure.

Experiments

All experiments were performed using a server on Ubuntu 22.04 LTS, equipped with an Intel(R) Xeon(R) Gold 6242 CPU and a cluster of NVIDIA A100 40GB GPUs. The source code for our experiments can be accessed at <https://github.com/yongkyung-oh/DualDynamics>.

Proposed method

The implicit component in our framework primarily utilizes Neural CDE, with Neural ODE and Neural SDE explored as alternatives in our ablation study. For the explicit component, we evaluated three distinct flow models: ResNet Flow, GRU Flow, and Coupling Flow. These flow architectures, as outlined by Biloš et al. (2021), were incorporated into our proposed framework. To assess the impact of using flow models, we also implemented a conventional multilayer perceptron (MLP) as a baseline for comparison. In practice, optimal flow model is selected by hyperparameter tuning process.

Benchmark methods

We employed a variety of benchmark models for classification and forecasting, incorporating conventional RNN (Rumelhart, Hinton, and Williams 1986; Medsker and Jain 1999), LSTM (Hochreiter and Schmidhuber 1997), and GRU (Chung et al. 2014), alongside their notable variants, including GRU- Δt (Choi et al. 2016), and GRU-D (Che et al. 2018). Also, we used attention-based method including transformer (Vaswani et al. 2017), Multi-Time Attention Networks (MTAN) (Shukla and Marlin 2021), and Multi-Integration Attention Module (MIAM) (Lee et al. 2022). ODE-based models like, GRU-ODE (De Brouwer et al. 2019), ODE-RNN (Rubanova, Chen, and Duvenaud 2019) ODE-LSTM (Lechner and Hasani 2020), Latent-ODE (Rubanova, Chen, and Duvenaud 2019), Augmented-ODE (Dupont, Doucet, and Teh 2019), and Attentive co-evolving neural ordinary differential equations (ACE-NODE) (Jhin et al. 2021) are considered. Furthermore, Neural CDE (Kidger et al. 2020), and Neural Rough Differential Equation (Neural RDE) (Morrill et al. 2021), were included in our comparative study. Additionally, recent advances in Neural CDE are considered, including Attentive Neural Controlled Differential Equation (ANCDE) (Jhin et al. 2024), EXtrapolation and InTerpolation-based model (EXIT) (Jhin et al. 2022), and LEArnable Path-based model (LEAP) (Jhin et al. 2023). Lastly, variations of Neural Flow (Biloš et al. 2021) are also included.

In the interpolation task, encoder-decoder architecture is implemented by Variational Auto-Encoder (VAE) scheme with the evidence lower bound (ELBO). RNN-VAE (Chen et al. 2018), L-ODE-RNN (Chen et al. 2018), L-ODE-ODE (Rubanova, Chen, and Duvenaud 2019), and mTAND-Full (MTAN encoder-MTAN decoder model) (Shukla and Marlin 2021), were used as benchmark methods, based on the suggestion of Shukla and Marlin (2021). In our model, the proposed method is utilized for the encoder component, while the conventional RNN is employed as the decoder.

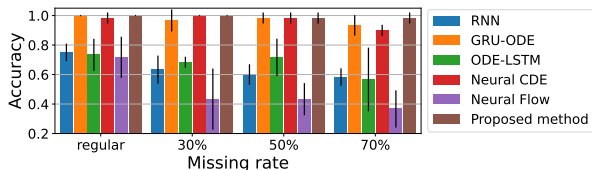
Robustness to dataset shift

To provide comprehensive insights, we conducted a descriptive analysis of model performances using the ‘BasicMotions’ dataset as a case study. We focused on

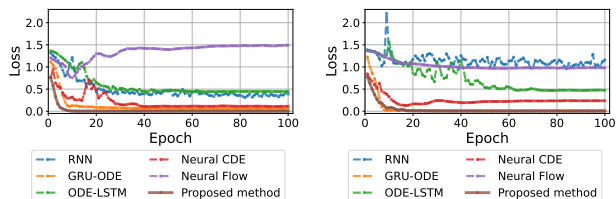
Table 1: Average classification performance on 18 datasets under regular and three missing rates (Values in parentheses show the average of 18 standard deviations. The **top-ranking** and **runner-up** choices are emphasized.

Methods	Regular		30% Missing		50% Missing		70% Missing		Average	
	Accuracy	Rank	Accuracy	Rank	Accuracy	Rank	Accuracy	Rank	Accuracy	Rank
RNN	0.560 (0.072)	11.9	0.484 (0.075)	14.7	0.471 (0.082)	14.0	0.453 (0.068)	14.4	0.492 (0.074)	13.8
LSTM	0.588 (0.067)	11.0	0.552 (0.075)	10.2	0.516 (0.073)	11.4	0.505 (0.067)	11.3	0.540 (0.071)	11.0
GRU	0.674 (0.080)	7.3	0.639 (0.065)	8.4	0.611 (0.076)	9.0	0.606 (0.088)	8.6	0.633 (0.077)	8.3
GRU- Δt	0.629 (0.065)	9.9	0.636 (0.069)	8.2	0.651 (0.068)	7.2	0.649 (0.074)	7.9	0.641 (0.069)	8.3
GRU-D	0.593 (0.088)	10.9	0.579 (0.087)	10.6	0.580 (0.075)	10.6	0.599 (0.062)	10.1	0.588 (0.078)	10.6
Transformer	0.720 (0.063)	6.8	0.663 (0.066)	8.0	0.669 (0.075)	7.4	0.643 (0.079)	8.2	0.674 (0.071)	7.6
MTAN	0.654 (0.088)	9.4	0.634 (0.098)	7.4	0.631 (0.089)	6.8	0.642 (0.073)	6.8	0.640 (0.087)	7.6
MIAM	0.573 (0.079)	11.9	0.585 (0.086)	10.0	0.572 (0.071)	9.9	0.544 (0.063)	11.1	0.568 (0.075)	10.7
GRU-ODE	0.663 (0.072)	7.6	0.661 (0.069)	7.4	0.664 (0.069)	6.8	0.659 (0.081)	6.9	0.662 (0.073)	<u>7.2</u>
ODE-RNN	0.652 (0.085)	7.3	0.632 (0.076)	7.8	0.626 (0.086)	7.8	0.653 (0.059)	<u>6.5</u>	0.641 (0.076)	7.4
ODE-LSTM	0.566 (0.074)	11.4	0.518 (0.069)	12.7	0.501 (0.068)	13.3	0.474 (0.068)	13.4	0.515 (0.070)	12.7
Neural CDE	0.681 (0.073)	7.6	0.672 (0.068)	7.4	0.661 (0.070)	7.3	0.652 (0.091)	7.3	0.667 (0.075)	7.4
Neural RDE	0.649 (0.082)	8.6	0.648 (0.071)	7.4	0.633 (0.078)	8.2	0.607 (0.079)	8.5	0.634 (0.078)	8.2
ANCDE	0.662 (0.083)	7.9	0.661 (0.083)	<u>7.1</u>	0.639 (0.080)	8.2	0.631 (0.073)	7.3	0.649 (0.080)	7.6
EXIT	0.595 (0.087)	10.1	0.580 (0.088)	10.5	0.578 (0.086)	10.1	0.564 (0.072)	10.4	0.579 (0.083)	10.3
LEAP	0.490 (0.062)	14.4	0.459 (0.070)	15.1	0.466 (0.074)	13.6	0.451 (0.074)	13.7	0.466 (0.070)	14.2
Neural Flow	0.545 (0.059)	11.9	0.485 (0.067)	13.4	0.455 (0.058)	14.3	0.438 (0.054)	14.1	0.481 (0.059)	13.4
Proposed method	0.724 (0.090)	5.1	0.720 (0.088)	4.9	0.691 (0.091)	5.1	0.697 (0.098)	4.6	0.708 (0.092)	4.9

five key methods: a standard RNN, GRU-ODE, ODE-LSTM, Neural CDE, Neural Flow, and our proposed method. Our investigation covered four different settings, including regular (0% missingness), and three missing rates including 30%, 50%, and 70%.



(a) Classification performance comparisons



(b) Test loss without missingness (regular)

(c) Test loss with 50% missing (irregular)

Figure 2: Performance and stability comparison using ‘BasicMotions’ dataset (monitoring for 100 epochs)

Figure 2 (a) illustrates the performance trend of each model concerning varying missing data rates. While the conventional RNN’s performance decreases as the missing rate increases, GRU-ODE and ODE-LSTM outperform conventional RNNs but become less stability with increasing missing data. Neural CDE demonstrates superior performance, whereas Neural Flow shows performance worse than that of the conventional RNN.

Our proposed method consistently demonstrates remarkable performance regardless of missing data rates.

Further exploration is presented in Figure 2 (b) and Figure 2 (c), illustrating the test loss dynamics of the ‘BasicMotions’ dataset, both with and without missingness. Despite its simplicity, Neural Flow shows limited convergence in both cases, whereas our proposed method achieves stability, outperforming both conventional approaches and Neural CDE. Furthermore, we included detailed results and computational time analysis in Supplementary material.

Table 2: Ablation study of the proposed method (Average of 18 standard deviations in parentheses)

Configuration	Accuracy	Loss
Proposed method (Neural CDE)	0.708 (0.092)	0.686 (0.168)
- Baseline	0.667 (0.075)	0.765 (0.264)
- Conventional MLP	0.582 (0.087)	0.862 (0.148)
- ResNet Flow	0.651 (0.091)	0.777 (0.155)
- GRU Flow	0.660 (0.079)	0.768 (0.172)
- Coupling Flow	0.669 (0.097)	0.747 (0.186)
Proposed method (Neural ODE)	0.535 (0.066)	0.968 (0.072)
- Baseline	0.502 (0.069)	0.981 (0.078)
- Conventional MLP	0.504 (0.066)	0.980 (0.076)
- ResNet Flow	0.510 (0.060)	0.978 (0.077)
- GRU Flow	0.523 (0.071)	0.981 (0.080)
- Coupling Flow	0.523 (0.064)	0.970 (0.070)
Proposed method (Neural SDE)	0.538 (0.066)	0.968 (0.071)
- Baseline	0.509 (0.061)	0.978 (0.073)
- Conventional MLP	0.506 (0.069)	0.981 (0.077)
- ResNet Flow	0.520 (0.064)	0.969 (0.073)
- GRU Flow	0.521 (0.068)	0.981 (0.073)
- Coupling Flow	0.519 (0.068)	0.975 (0.079)

Based on our initial findings, we extended our experiments to 18 public benchmark datasets from the the University of East Anglia (UEA) and the University of California Riverside (UCR) Time Series Classification Repository (Bagnall et al. 2018; Dau et al. 2019), encompassing Motion & Human Activity Recognition (HAR), Electrocardiogram (ECG) & Electroencephalogram (EEG), and Sensor domains. Following Kidger et al. (2020) and Oh, Lim, and Kim (2024), we generated subsets with 30%, 50%, and 70% missingness rates, creating four distinct scenarios. Data was split

Table 3: Performance of interpolation relative to observed percentage on the PhysioNet Mortality dataset

Methods	Test MSE $\times 10^{-3}$				
	50%	60%	70%	80%	90%
RNN-VAE	13.418 \pm 0.008	12.594 \pm 0.004	11.887 \pm 0.005	11.133 \pm 0.007	11.470 \pm 0.006
L-ODE-RNN	8.132 \pm 0.020	8.140 \pm 0.018	8.171 \pm 0.030	8.143 \pm 0.025	8.402 \pm 0.022
L-ODE-ODE	6.721 \pm 0.109	6.816 \pm 0.045	6.798 \pm 0.143	6.850 \pm 0.066	7.142 \pm 0.066
mTAND-Full	4.139 \pm 0.029	4.018 \pm 0.048	4.157 \pm 0.053	4.410 \pm 0.149	4.798 \pm 0.036
Proposed method	3.631 \pm 0.049	3.659 \pm 0.028	3.463 \pm 0.032	3.224 \pm 0.044	3.114 \pm 0.050

70:15:15 for training, validation, and testing. We employed five-fold cross-validation, evaluating mean performance and ranking across folds. For dataset details and implementation specifics, refer to the Supplementary material and the corresponding repository³.

In the results presented in Table 1, our method distinctly stands out, demonstrating superiority when compared with other contemporary techniques. Considering the volatile nature of accuracy scores across diverse datasets, we prioritize rank statistics as a more consistent metric for comparative analysis. Across the four missing rate scenarios considered, our proposed method consistently achieves top-tier accuracy, confirming its robustness and effectiveness.

We conducted an in-depth comparative analysis of the classification efficacy and cross-entropy loss across various flow model designs, as detailed in Table 2. For implicit component, Neural CDE outperformed compared to Neural ODE and Neural SDE. The proposed method selected the flow configuration from ResNet flow, GRU flow, and Coupling flow during hyperparameter tuning. For the comparison, we employed conventional Multi-layer Perceptrons (MLPs), which notably failed to meet specific flow criteria, including invertibility. Empirical evaluations indicate that the performance of conventional MLP is worse compared to the flow-based approach. This observation confirms the superiority of our proposed method.

Interpolation for the missing data

The interpolation experiment utilized the 2012 PhysioNet Mortality dataset (Silva et al. 2012), comprising 37 variables from ICU records over 48 hours post-admission. Following Rubanova, Chen, and Duvenaud (2019), timestamps were adjusted to the nearest minute, yielding up to 2880 intervals per series. We adhered to Shukla and Marlin (2021)’s methodology, varying observation frequency from 50% to 90% to predict remaining samples using 8000 instances. In our interpolation experiments, we followed the experimental protocol advocated by Shukla and Marlin (2021). This strategy involved generating interpolated values based on a selected subset of data points to predict values for the unobserved time intervals. The interpolation spanned an observational range from 50% to 90% of the total data points. During the test phase, models were designed to interpolate values for the remaining intervals

in the test set. The efficacy of the models was quantitatively assessed using Mean Squared Error (MSE), supported by five cross-validations.

Table 3 demonstrates that the interpolation performance of our proposed methods is superior compared to the benchmark models across all three flow configurations. The flow configuration achieved lower MSE errors compared to the non-flow neural network, a consistent and robust observation across various levels of observed data, ranging from 50% to 90%. Detailed experiment protocols and results are included in Supplementary material.

Classification of irregularly-sampled data

We utilized the PhysioNet Sepsis dataset (Reyna et al. 2019), comprising 40,335 patient instances with 34 temporal variables. Following Kidger et al. (2020), we addressed data irregularity using two classification approaches: with and without observation intensity (OI). Observation intensity (OI) indicates patient condition severity, augmenting each time series point with an intensity index when utilized. Model performance was evaluated using Area Under the Receiver Operating Characteristic Curve (AUROC), with benchmark comparisons from Jhin et al. (2022).

In Table 4, our method demonstrates superior AUROC scores in both scenarios. Consistent with prior experimental findings, models based on flow exhibit enhanced efficacy relative to their non-flow neural network counterparts. These results confirm the effectiveness of our proposed methodologies in addressing challenges associated with time series irregularity and missingness.

Table 4: AUROC on PhysioNet Sepsis dataset

Methods	Test AUROC		Memory (MB)	
	OI	No OI	OI	No OI
GRU- Δt	0.878 \pm 0.006	0.840 \pm 0.007	837	826
GRU-D	0.871 \pm 0.022	0.850 \pm 0.013	889	878
GRU-ODE	0.852 \pm 0.010	0.771 \pm 0.024	454	273
ODE-RNN	0.874 \pm 0.016	0.833 \pm 0.020	696	686
Latent-ODE	0.787 \pm 0.011	0.495 \pm 0.002	133	126
ACE-NODE	0.804 \pm 0.010	0.514 \pm 0.003	194	218
Neural CDE	0.880 \pm 0.006	0.776 \pm 0.009	244	122
ANCDE	0.900 \pm 0.002	0.823 \pm 0.003	285	129
EXIT	0.913 \pm 0.002	0.836 \pm 0.003	257	127
Proposed method	0.918 \pm 0.003	0.873 \pm 0.004	453	233

Forecasting with the partial observations

We utilized two datasets, MuJoCo and Google, with different levels of observation for the forecasting task.

³<https://github.com/yongkyung-oh/torch-ists>

Table 5: Forecasting performance on MuJoCo dataset

Methods	Test MSE			
	Regular	30% dropped	50% dropped	70% dropped
GRU- Δt	0.223 \pm 0.020	0.198 \pm 0.036	0.193 \pm 0.015	0.196 \pm 0.028
GRU-D	0.578 \pm 0.042	0.608 \pm 0.032	0.587 \pm 0.039	0.579 \pm 0.052
GRU-ODE	0.856 \pm 0.016	0.857 \pm 0.015	0.852 \pm 0.015	0.861 \pm 0.015
ODE-RNN	0.328 \pm 0.225	0.274 \pm 0.213	0.237 \pm 0.110	0.267 \pm 0.217
Latent-ODE	0.029 \pm 0.011	0.056 \pm 0.001	0.055 \pm 0.004	0.058 \pm 0.003
Augmented-ODE	0.055 \pm 0.004	0.056 \pm 0.004	0.057 \pm 0.005	0.057 \pm 0.005
ACE-NODE	0.039 \pm 0.003	0.053 \pm 0.007	0.053 \pm 0.005	0.052 \pm 0.006
Neural CDE	0.028 \pm 0.002	0.027 \pm 0.000	0.027 \pm 0.001	0.026 \pm 0.001
ANCDE	0.026 \pm 0.001	0.025 \pm 0.001	0.025 \pm 0.001	0.024 \pm 0.001
EXIT	0.026 \pm 0.000	0.025 \pm 0.004	0.026 \pm 0.000	0.026 \pm 0.001
LEAP	0.022 \pm 0.002	0.022 \pm 0.001	0.022 \pm 0.002	0.022 \pm 0.001
Proposed method	0.006 \pm 0.001	0.008 \pm 0.001	0.008 \pm 0.001	0.008 \pm 0.001

Table 6: Forecasting performance on Google dataset

Methods	Test MSE			
	Regular	30% dropped	50% dropped	70% dropped
GRU- Δt	0.0406 \pm 0.002	0.0043 \pm 0.003	0.0041 \pm 0.002	0.0041 \pm 0.001
GRU-D	0.0040 \pm 0.004	0.0058 \pm 0.018	0.0039 \pm 0.001	0.0040 \pm 0.001
GRU-ODE	0.0028 \pm 0.016	0.0029 \pm 0.001	0.0031 \pm 0.004	0.0030 \pm 0.002
ODE-RNN	0.0311 \pm 0.044	0.0318 \pm 0.066	0.0322 \pm 0.056	0.0324 \pm 0.053
Latent-ODE	0.0030 \pm 0.011	0.0032 \pm 0.001	0.0033 \pm 0.002	0.0032 \pm 0.003
Augmented-ODE	0.0023 \pm 0.002	0.0025 \pm 0.002	0.0029 \pm 0.006	0.0023 \pm 0.005
ACE-NODE	0.0022 \pm 0.003	0.0024 \pm 0.001	0.0022 \pm 0.002	0.0025 \pm 0.002
Neural CDE	0.0037 \pm 0.062	0.0038 \pm 0.073	0.0032 \pm 0.035	0.0039 \pm 0.038
ANCDE	0.0020 \pm 0.002	0.0022 \pm 0.001	0.0021 \pm 0.002	0.0021 \pm 0.001
EXIT	0.0016 \pm 0.002	0.0016 \pm 0.001	0.0017 \pm 0.001	0.0019 \pm 0.003
Proposed method	0.0010 \pm 0.0001	0.0010 \pm 0.0001	0.0009 \pm 0.0001	0.0013 \pm 0.0002

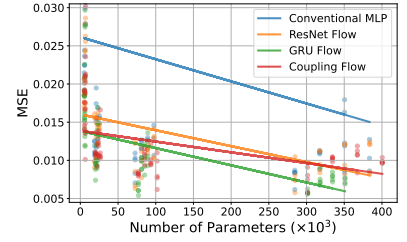


Figure 3: Forecasting performance versus the number of parameters on MuJoCo with regular scenario

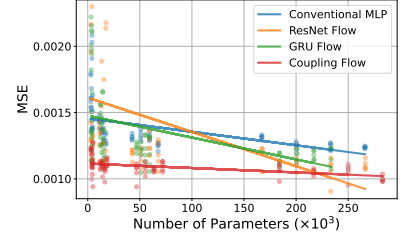


Figure 4: Forecasting performance versus the number of parameters on Google with regular scenario

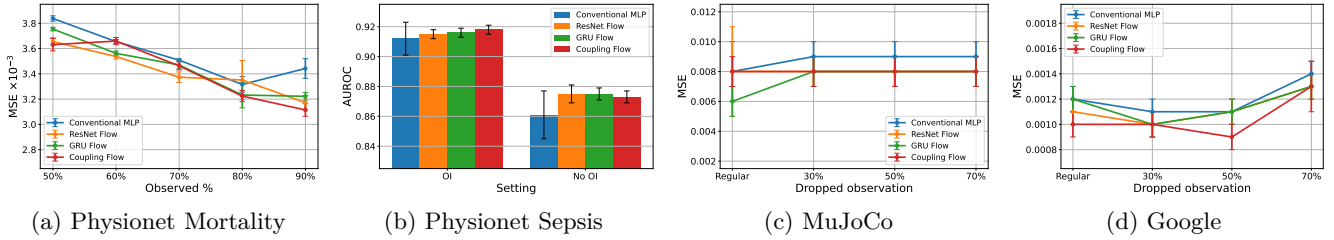


Figure 5: Ablation study of different flow model configurations

Detailed explanations of each dataset and results are provided in Supplementary material.

MuJoCo. We utilized the MuJoCo dataset (Todorov, Erez, and Tassa 2012), based on the Hopper configuration from the DeepMind control suite (Tassa et al. 2018). Following Jhin et al. (2023, 2024), we used 50 initial points to predict the next 10, introducing 30%, 50%, and 70% missing data scenarios. Table 5 illustrates the forecasting performance across diverse conditions, with our method consistently demonstrating minimal MSE.

Google. We used the Google stock data (2011-2021)(Jhin et al. 2022), forecasting 5 price metrics for the next 10 days based on 50 days of history. Following Jhin et al. (2022)’s protocol, we introduced 30%, 50%, and 70% missing data scenarios. Table 6 presents the outcomes of forecasting stock data with partial observations. When comparing with benchmark methods, our method consistently presents lower MSE in the four different scenarios.

Discussion

Performance versus network capacity. Our analysis reveals that the performance improvements of DualDynamics are not merely a result of increased network capacity, but rather stem from the synergistic integration of implicit and explicit methods in our model architecture. To validate DualDynamics’ effectiveness, we conducted controlled experiments comparing it against models with similar parameter counts. Figures 3 and 4 illustrate the relationship between parameter count and MSE for our flow architecture versus conventional MLPs. Figure 3 shows that increasing MLP capacity yields limited improvement on the MuJoCo dataset, while DualDynamics maintains superior performance. Figure 4 demonstrates that with optimal flow configuration, DualDynamics consistently outperforms MLPs on the Google dataset across all model sizes.

This performance advantage persists even when adjusting baseline model complexity to match DualDynamics, indicating that our framework’s superiority

stems from its architectural design rather than increased computational resources. These results highlight DualDynamics’ efficiency in capturing complex temporal dynamics in irregular time series data.

Ablation study of flow configurations. Figure 5 presents a comprehensive overview of our ablation study, illustrating the performance of various flow configurations across different tasks, as detailed in the preceding sections. The results demonstrate a clear advantage of flow-based architectures over the conventional MLP approach, refer to the detailed results in the Supplementary material. These results suggest that incorporating implicit and explicit could lead to significant improvements in model performance and capabilities.

Variations in our framework. Our framework’s architecture allows for several potential variations, each with distinct trade-offs. One possible modification is to utilize only $z(t)$ instead of $\hat{z}(t)$ after training the unified framework. However, this approach significantly limits the model’s expressiveness, as it fails to leverage the unique properties of the flow model. Another consideration is the replacement of the flow model with more sophisticated architectures, such as feedforward networks (Hornik, Stinchcombe, and White 1989), gated recurrent units (Chung et al. 2014), temporal convolutional networks (Lea et al. 2017), or transformer-based attention mechanisms (Vaswani et al. 2017). For further details and quantitative comparisons, we refer the reader to the Supplementary material.

Conclusion

We introduce DualDynamics, an innovative methodology that integrates implicit and explicit methods for modeling irregularly-sampled time series data. This sophisticated paradigm excels in capturing intricate temporal characteristics inherent in continuous-time processes, offering an enhanced framework for representation learning in time series analysis. By synergistically combining these approaches, our method strikes a balance between expressive power and computational efficiency, addressing key challenges in temporal modeling.

Our approach consistently surpasses existing benchmarks in classification, interpolation, and forecasting tasks, significantly elevating the precision and depth of understanding in temporal dynamics. These outstanding results highlight DualDynamics’ potential for diverse real-world applications. Its adaptability to various temporal modeling challenges positions it as a significant advancement in irregular time series analysis.

Ethic Statement

We commit to conducting our research with integrity, ensuring ethical practices and responsible use of technology in alignment with established academic and scientific standards.

Reproducibility Statement

We make our code and implementation details publicly accessible for reproducibility purposes. Code is available at <https://github.com/yongkyung-oh/DualDynamics>.

Acknowledgments

We thank the teams and individuals for their efforts in dataset preparation and curation for our research, especially the UEA & UCR repository for the numerous datasets we extensively analyzed.

This research was supported by Basic Science Research Program through the National Research Foundation of Korea (NRF) funded by the Ministry of Education (RS-2024-00407852); Korea Health Technology R&D Project through the Korea Health Industry Development Institute (KHIDI), funded by the Ministry of Health and Welfare, Republic of Korea (HI19C1095); the Institute of Information & communications Technology Planning & Evaluation (IITP) grant funded by the Korea government (MSIT) (No.2020-0-01336, Artificial Intelligence Graduate School Program (UNIST)); and the Institute of Information & communications Technology Planning & Evaluation (IITP) grant funded by the Korea government (MSIT) (No.RS-2021-II212068, Artificial Intelligence Innovation Hub).

References

- Adams, R. P.; Pennington, J.; Johnson, M. J.; Smith, J.; Ovadia, Y.; Patton, B.; and Saunderson, J. 2018. Estimating the spectral density of large implicit matrices. *arXiv preprint arXiv:1802.03451*.
- Bagnall, A.; Dau, H. A.; Lines, J.; Flynn, M.; Large, J.; Bostrom, A.; Southam, P.; and Keogh, E. 2018. The UEA multivariate time series classification archive, 2018. *arXiv preprint arXiv:1811.00075*.
- Behrmann, J.; Grathwohl, W.; Chen, R. T.; Duvenaud, D.; and Jacobsen, J.-H. 2019. Invertible residual networks. In *International Conference on Machine Learning*, 573–582. PMLR.
- Biloš, M.; Sommer, J.; Rangapuram, S. S.; Januschowski, T.; and Günnemann, S. 2021. Neural flows: Efficient alternative to neural ODEs. *Advances in Neural Information Processing Systems*, 34: 21325–21337.
- Chalvidal, M.; Ricci, M.; Vanrullen, R.; and Serre, T. 2021. Go with the Flow: Adaptive Control for Neural ODEs. In *ICLR 2021: International Conference on Learning Representations*.
- Che, Z.; Purushotham, S.; Cho, K.; Sontag, D.; and Liu, Y. 2018. Recurrent neural networks for multivariate time series with missing values. *Scientific Reports*, 8(1): 6085.
- Chen, R. T.; Rubanova, Y.; Bettencourt, J.; and Duvenaud, D. K. 2018. Neural ordinary differential equations. *Advances in neural information processing systems*, 31.
- Choi, E.; Bahadori, M. T.; Schuetz, A.; Stewart, W. F.; and Sun, J. 2016. Doctor ai: Predicting clinical events via recurrent neural networks. In *Machine learning for healthcare conference*, 301–318. PMLR.
- Chung, J.; Gulcehre, C.; Cho, K.; and Bengio, Y. 2014. Empirical evaluation of gated recurrent neural networks on sequence modeling. *arXiv preprint arXiv:1412.3555*.

- Dau, H. A.; Bagnall, A.; Kamgar, K.; Yeh, C.-C. M.; Zhu, Y.; Gharghabi, S.; Ratanamahatana, C. A.; and Keogh, E. 2019. The UCR time series archive. *IEEE/CAA Journal of Automatica Sinica*, 6(6): 1293–1305.
- De Brouwer, E.; Simm, J.; Arany, A.; and Moreau, Y. 2019. GRU-ODE-Bayes: Continuous modeling of sporadically-observed time series. *Advances in neural information processing systems*, 32.
- Dinh, L.; Krueger, D.; and Bengio, Y. 2014. Nice: Non-linear independent components estimation. *arXiv preprint arXiv:1410.8516*.
- Dinh, L.; Sohl-Dickstein, J.; and Bengio, S. 2016. Density estimation using real nvp. *arXiv preprint arXiv:1605.08803*.
- Dupont, E.; Doucet, A.; and Teh, Y. W. 2019. Augmented neural odes. *Advances in Neural Information Processing Systems*, 32.
- Gao, Y.; and Lin, J. 2018. Efficient discovery of variable-length time series motifs with large length range in million scale time series. *arXiv preprint arXiv:1802.04883*.
- Gouk, H.; Frank, E.; Pfahringer, B.; and Cree, M. J. 2021. Regularisation of neural networks by enforcing lipschitz continuity. *Machine Learning*, 110: 393–416.
- Grathwohl, W.; Chen, R. T.; Bettencourt, J.; Sutskever, I.; and Duvenaud, D. 2018. Fjord: Free-form continuous dynamics for scalable reversible generative models. *arXiv preprint arXiv:1810.01367*.
- Han, I.; Malioutov, D.; and Shin, J. 2015. Large-scale log-determinant computation through stochastic Chebyshev expansions. In *International Conference on Machine Learning*, 908–917. PMLR.
- He, K.; Zhang, X.; Ren, S.; and Sun, J. 2016. Deep residual learning for image recognition. In *Proceedings of the IEEE conference on computer vision and pattern recognition*, 770–778.
- He, Y.; and Semnani, S. J. 2023. Incremental Neural Controlled Differential Equations for Modeling of Path-dependent Materials. *arXiv preprint arXiv:2311.17336*.
- Hochreiter, S.; and Schmidhuber, J. 1997. Long short-term memory. *Neural computation*, 9(8): 1735–1780.
- Hornik, K.; Stinchcombe, M.; and White, H. 1989. Multilayer feedforward networks are universal approximators. *Neural networks*, 2(5): 359–366.
- Hutchinson, M. F. 1989. A stochastic estimator of the trace of the influence matrix for Laplacian smoothing splines. *Communications in Statistics-Simulation and Computation*, 18(3): 1059–1076.
- Irie, K.; Faccio, F.; and Schmidhuber, J. 2022. Neural differential equations for learning to program neural nets through continuous learning rules. *Advances in Neural Information Processing Systems*, 35: 38614–38628.
- Jhin, S. Y.; Jo, M.; Kong, T.; Jeon, J.; and Park, N. 2021. Ace-node: Attentive co-evolving neural ordinary differential equations. In *Proceedings of the 27th ACM SIGKDD Conference on Knowledge Discovery & Data Mining*, 736–745.
- Jhin, S. Y.; Jo, M.; Kook, S.; Park, N.; Woo, S.; and Lim, S. 2023. Learnable Path in Neural Controlled Differential Equations. *arXiv preprint arXiv:2301.04333*.
- Jhin, S. Y.; Lee, J.; Jo, M.; Kook, S.; Jeon, J.; Hyeong, J.; Kim, J.; and Park, N. 2022. Exit: Extrapolation and interpolation-based neural controlled differential equations for time-series classification and forecasting. In *Proceedings of the ACM Web Conference 2022*, 3102–3112.
- Jhin, S. Y.; Shin, H.; Kim, S.; Hong, S.; Jo, M.; Park, S.; Park, N.; Lee, S.; Maeng, H.; and Jeon, S. 2024. Attentive neural controlled differential equations for time-series classification and forecasting. *Knowledge and Information Systems*, 66(3): 1885–1915.
- Jia, J.; and Benson, A. R. 2019. Neural jump stochastic differential equations. *Advances in Neural Information Processing Systems*, 32.
- Keogh, E. 2003. Efficiently finding arbitrarily scaled patterns in massive time series databases. In *European Conference on Principles of Data Mining and Knowledge Discovery*, 253–265. Springer.
- Kidger, P. 2022. On neural differential equations. *arXiv preprint arXiv:2202.02435*.
- Kidger, P.; Chen, R. T.; and Lyons, T. J. 2021. "Hey, that's not an ODE": Faster ODE Adjoints via Seminorms. In *ICML*, 5443–5452.
- Kidger, P.; Morrill, J.; Foster, J.; and Lyons, T. 2020. Neural controlled differential equations for irregular time series. *Advances in Neural Information Processing Systems*, 33: 6696–6707.
- Kingma, D. P.; and Dhariwal, P. 2018. Glow: Generative flow with invertible 1x1 convolutions. *Advances in neural information processing systems*, 31.
- Kobyzev, I.; Prince, S. J.; and Brubaker, M. A. 2020. Normalizing flows: An introduction and review of current methods. *IEEE transactions on pattern analysis and machine intelligence*, 43(11): 3964–3979.
- Lea, C.; Flynn, M. D.; Vidal, R.; Reiter, A.; and Hager, G. D. 2017. Temporal convolutional networks for action segmentation and detection. In *proceedings of the IEEE Conference on Computer Vision and Pattern Recognition*, 156–165.
- Lechner, M.; and Hasani, R. 2020. Learning long-term dependencies in irregularly-sampled time series. *arXiv preprint arXiv:2006.04418*.
- Lee, Y.; Jun, E.; Choi, J.; and Suk, H.-I. 2022. Multi-view Integrative Attention-based Deep Representation Learning for Irregular Clinical Time-series Data. *IEEE Journal of Biomedical and Health Informatics*.
- Li, J.; and Chen, J. 2008. The principle of preservation of probability and the generalized density evolution equation. *Structural Safety*, 30(1): 65–77.
- Li, X.; Wong, T.-K. L.; Chen, R. T.; and Duvenaud, D. 2020. Scalable gradients for stochastic differential equations. In *International Conference on Artificial Intelligence and Statistics*, 3870–3882. PMLR.
- Liaw, R.; Liang, E.; Nishihara, R.; Moritz, P.; Gonzalez, J. E.; and Stoica, I. 2018. Tune: A Research Platform for Distributed Model Selection and Training. *arXiv preprint arXiv:1807.05118*.
- Löning, M.; Bagnall, A.; Ganesh, S.; Kazakov, V.; Lines, J.; and Király, F. J. 2019. sktime: A unified interface for machine learning with time series. *arXiv preprint arXiv:1909.07872*.
- Lu, Y.; Zhong, A.; Li, Q.; and Dong, B. 2018. Beyond finite layer neural networks: Bridging deep architectures and numerical differential equations. In *International Conference on Machine Learning*, 3276–3285. PMLR.
- Massaroli, S.; Poli, M.; Bin, M.; Park, J.; Yamashita, A.; and Asama, H. 2020a. Stable neural flows. *arXiv preprint arXiv:2003.08063*.

- Massaroli, S.; Poli, M.; Park, J.; Yamashita, A.; and Asama, H. 2020b. Dissecting neural odes. *Advances in Neural Information Processing Systems*, 33: 3952–3963.
- Medsker, L.; and Jain, L. C. 1999. *Recurrent neural networks: design and applications*. CRC press.
- Moritz, P.; Nishihara, R.; Wang, S.; Tumanov, A.; Liaw, R.; Liang, E.; Elibol, M.; Yang, Z.; Paul, W.; Jordan, M. I.; et al. 2018. Ray: A distributed framework for emerging {AI} applications. In *13th {USENIX} Symposium on Operating Systems Design and Implementation ({OSDI} 18)*, 561–577.
- Morrill, J.; Kidger, P.; Yang, L.; and Lyons, T. 2022. On the choice of interpolation scheme for neural CDEs. *Transactions on Machine Learning Research*, 2022(9).
- Morrill, J.; Salvi, C.; Kidger, P.; and Foster, J. 2021. Neural rough differential equations for long time series. In *International Conference on Machine Learning*, 7829–7838. PMLR.
- Norcliffe, A.; Bodnar, C.; Day, B.; Moss, J.; and Liò, P. 2020. Neural ODE Processes. In *International Conference on Learning Representations*.
- Oh, Y.; Lim, D.; and Kim, S. 2024. Stable Neural Stochastic Differential Equations in Analyzing Irregular Time Series Data. In *The Twelfth International Conference on Learning Representations*.
- Onken, D.; Fung, S. W.; Li, X.; and Ruthotto, L. 2021. Ot-flow: Fast and accurate continuous normalizing flows via optimal transport. In *Proceedings of the AAAI Conference on Artificial Intelligence*, volume 35, 9223–9232.
- Pal, S.; Zeng, Z.; Ravi, S. N.; and Singh, V. 2023. Controlled differential equations on long sequences via non-standard wavelets. In *International Conference on Machine Learning*, 26820–26836. PMLR.
- Papamakarios, G.; Nalisnick, E.; Rezende, D. J.; Mohamed, S.; and Lakshminarayanan, B. 2021. Normalizing flows for probabilistic modeling and inference. *The Journal of Machine Learning Research*, 22(1): 2617–2680.
- Paszke, A.; Gross, S.; Massa, F.; Lerer, A.; Bradbury, J.; Chanan, G.; Killeen, T.; Lin, Z.; Gimelshein, N.; Antiga, L.; et al. 2019. Pytorch: An imperative style, high-performance deep learning library. *Advances in neural information processing systems*, 32.
- Pollini, N.; Lavan, O.; and Amir, O. 2018. Adjoint sensitivity analysis and optimization of hysteretic dynamic systems with nonlinear viscous dampers. *Structural and Multidisciplinary Optimization*, 57: 2273–2289.
- Pontryagin, L. S. 2018. *Mathematical theory of optimal processes*. Routledge.
- Reyna, M. A.; Josef, C.; Seyedi, S.; Jeter, R.; Shashikumar, S. P.; Westover, M. B.; Sharma, A.; Nemat, S.; and Clifford, G. D. 2019. Early prediction of sepsis from clinical data: the PhysioNet/Computing in Cardiology Challenge 2019. In *2019 Computing in Cardiology (CinC)*, Page–1. IEEE.
- Rubanova, Y.; Chen, R. T.; and Duvenaud, D. K. 2019. Latent ordinary differential equations for irregularly-sampled time series. *Advances in neural information processing systems*, 32.
- Rumelhart, D. E.; Hinton, G. E.; and Williams, R. J. 1986. Learning representations by back-propagating errors. *nature*, 323(6088): 533–536.
- Shukla, S. N.; and Marlin, B. M. 2021. Multi-time attention networks for irregularly sampled time series. *arXiv preprint arXiv:2101.10318*.
- Silva, I.; Moody, G.; Scott, D. J.; Celi, L. A.; and Mark, R. G. 2012. Predicting in-hospital mortality of icu patients: The physionet/computing in cardiology challenge 2012. In *2012 Computing in Cardiology*, 245–248. IEEE.
- Sonoda, S.; and Murata, N. 2019. Transport analysis of infinitely deep neural network. *The Journal of Machine Learning Research*, 20(1): 31–82.
- Tan, C. W.; Petitjean, F.; Keogh, E.; and Webb, G. I. 2019. Time series classification for varying length series. *arXiv preprint arXiv:1910.04341*.
- Tassa, Y.; Doron, Y.; Muldal, A.; Erez, T.; Li, Y.; Casas, D. d. L.; Budden, D.; Abdolmaleki, A.; Merel, J.; Lefrancq, A.; et al. 2018. Deepmind control suite. *arXiv preprint arXiv:1801.00690*.
- Todorov, E.; Erez, T.; and Tassa, Y. 2012. Mujoco: A physics engine for model-based control. In *2012 IEEE/RSJ international conference on intelligent robots and systems*, 5026–5033. IEEE.
- Vaswani, A.; Shazeer, N.; Parmar, N.; Uszkoreit, J.; Jones, L.; Gomez, A. N.; Kaiser, Ł.; and Polosukhin, I. 2017. Attention is all you need. *Advances in neural information processing systems*, 30.
- Westny, T.; Mohammadi, A.; Jung, D.; and Frisk, E. 2023. Stability-Informed Initialization of Neural Ordinary Differential Equations. *arXiv preprint arXiv:2311.15890*.
- Yankov, D.; Keogh, E.; Medina, J.; Chiu, B.; and Zordan, V. 2007. Detecting time series motifs under uniform scaling. In *Proceedings of the 13th ACM SIGKDD international conference on Knowledge discovery and data mining*, 844–853.

Experiment details

We consider following experiments: (1) Interpolation for the missing data, (2) Classification of irregularly-sampled data, and (3) Forecasting with the partial observations. All experiments were performed using a server on Ubuntu 22.04 LTS, equipped with an Intel(R) Xeon(R) Gold 6242 CPU and multiple NVIDIA A100 40GB GPUs. The source code for our experiments can be accessed at <https://github.com/yongkyung-oh/DualDynamics>.

Figure 6 illustrates the architecture of our proposed DualDynamics. This framework integrates implicit and explicit learning components for enhanced time series modeling. The implicit component can be implemented using Neural ODEs, Neural CDEs, or Neural SDEs, each adept at capturing complex temporal dependencies. The explicit component, designed to refine these representations, utilizes advanced neural flow models: ResNet Flow, GRU Flow, or Coupling Flow. This combination of implicit and explicit methods in DualDynamics aims to balance flexibility in modeling irregular time series with computational efficiency, potentially improving performance.

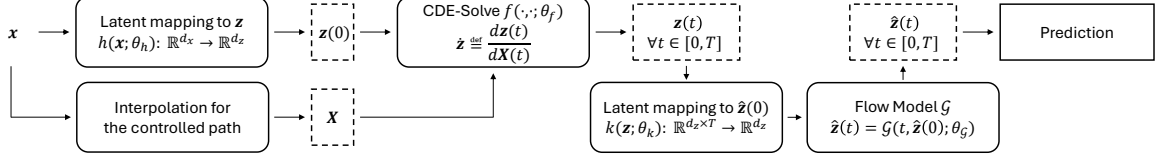


Figure 6: The detailed architecture of the proposed DualDynamics with Neural CDE

Implicit component: NDE-based approaches

Neural ODEs Let $\mathbf{x} = (x_0, x_1, \dots, x_n)$ be a vector of original (possibly, irregularly-sampled) observations. For a given time t , let us denote a latent state as $\mathbf{z}(t)$. Neural ODEs can be formally expressed as:

$$\mathbf{z}(t) = \mathbf{z}(0) + \int_0^t f(s, \mathbf{z}(s); \theta_f) ds, \quad (20)$$

with the initial condition $\mathbf{z}(0) = h(\mathbf{x}; \theta_h)$ where $h: \mathbb{R}^{d_x} \rightarrow \mathbb{R}^{d_z}$ is an affine function with parameter θ_h . In Eq. (20), the function $h(\cdot; \theta_h)$ can capture the intrinsic features from the input to the latent state. $f(s, \mathbf{z}(s); \theta_f)$, which approximates the rate of change, $\dot{\mathbf{z}} \equiv \frac{d\mathbf{z}(t)}{dt}$, is modelled using a neural network parameterized by θ_f . However, the performance of Neural ODEs often diminishes due to their dependence on initial conditions (Kidger 2022).

Neural CDEs Neural CDEs provide a framework for constructing a continuous-time representation by formulating a controlled path $X(t)$, generated through natural cubic spline interpolation of observed data (Kidger et al. 2020). The Neural CDEs is expressed via the Riemann–Stieltjes integral:

$$\mathbf{z}(t) = \mathbf{z}(0) + \int_0^t f(s, \mathbf{z}(s); \theta_f) dX(s), \quad (21)$$

with the initial condition $\mathbf{z}(0) = h(x_0; \theta_h)$ where $f(s, \mathbf{z}(s); \theta_f)$ provides an approximation to $\frac{d\mathbf{z}(t)}{dX(t)}$, differentiating Neural CDEs from Neural ODEs in their approximation approach. To evaluate the integral in Eq. (21), one may utilize the conventional ODE solvers by recognizing that $\dot{\mathbf{z}}(t) \equiv \frac{d\mathbf{z}(t)}{dX(t)}$.

Neural SDEs Neural SDEs extend the concept of Neural ODEs by incorporating a stochastic term to model uncertainty and noise in the dynamics (Oh, Lim, and Kim 2024). For a given time t and latent state $\mathbf{z}(t)$, Neural SDEs can be formally expressed as:

$$\mathbf{z}(t) = \mathbf{z}(0) + \int_0^t f(s, \mathbf{z}(s); \theta_f) ds + \int_0^t g(s, \mathbf{z}(s); \theta_g) dW(s), \quad (22)$$

with the initial condition $\mathbf{z}(0) = h(\mathbf{x}; \theta_h)$ where $h: \mathbb{R}^{d_x} \rightarrow \mathbb{R}^{d_z}$ is an affine function with parameter θ_h , similar to Neural ODEs. Here, $f(t, \mathbf{z}(t); \theta_f)$ represents the drift term, which models the deterministic part of the dynamics, while $g(t, \mathbf{z}(t); \theta_g)$ is the diffusion term that captures the stochastic component. $W(t)$ denotes a standard Wiener process (Brownian motion). In Eq. (22), both f and g are modeled using neural networks parameterized by θ_f and θ_g , respectively. Neural SDEs provide a framework for modeling complex, stochastic temporal dynamics, allowing for the representation of uncertainty in the latent state evolution.

Explicit component: flow model configurations

We integrate three distinct flow architectures proposed in Biloš et al. (2021) within the proposed framework.

ResNet flow. Originating from the concept of Residual Networks (ResNets) (He et al. 2016), the ResNet flow model can be conceptualized as a continuous-time analogue of ResNets. The core dynamics of $\mathbf{z}(t)$ in ResNet flow are described by the equation:

$$\mathcal{G}(t, \mathbf{z}) = \mathbf{z} + \varphi(t)g(t, \mathbf{z}), \quad (23)$$

where φ represents a temporal embedding function and g denotes a continuous, nonlinear transformation parameterized by θ_g . To address the inherent non-invertibility in standard ResNets, spectral normalization techniques (Gouk et al. 2021) are employed, ensuring a bounded Lipschitz constant and thus, invertibility (Behrmann et al. 2019).

GRU flow. The GRU flow model extends the Gated Recurrent Unit (GRU) architecture (Chung et al. 2014) to a continuous-time setting. In this model, the hidden state \mathbf{z} evolves continuously according to an ordinary differential equation, akin to the updates in traditional discrete GRUs. De Brouwer et al. (2019) introduced GRU-ODE, and Biloš et al. (2021) further refined it to an invertible form within the Neural Flow context, as expressed by:

$$\mathcal{G}(t, \mathbf{z}) = \mathbf{z} + \varphi(t)(1 - g_1(t, \mathbf{z})) \odot (g_2(t, \mathbf{z}) - \mathbf{z}), \quad (24)$$

where $\varphi(t)$ is a time-dependent embedding function, and g_1, g_2 are adapted from the GRU, where $g_1(t, \mathbf{z}) = \alpha \cdot \text{sigmoid}(f_1(t, \mathbf{z}))$, and $g_2(t, \mathbf{z}) = \text{tanh}(f_2(t, g_3(t, \mathbf{z}) \odot \mathbf{z}))$, and $g_3(t, \mathbf{z}) = \beta \cdot \text{sigmoid}(f_3(t, \mathbf{z}))$. f_1, f_2, f_3 are any arbitrary neural networks.

Coupling flow. The concept of Coupling flow, initially introduced by Dinh, Krueger, and Bengio (2014) and Dinh, Sohl-Dickstein, and Bengio (2016), involves a bijective transformation characterized by its computational efficiency and flexibility. Input dimensions are partitioned into two disjoint subsets d_1 and d_2 , leading to the transformation:

$$\mathcal{G}(t)_{d_1} = \mathbf{z}_{d_1} \exp(u(t, \mathbf{z}_{d_2})\varphi_u(t)) + v(t, \mathbf{z}_{d_2})\varphi_v(t), \quad (25)$$

with u and v as neural networks, and φ_u, φ_v as time-dependent embedding functions. Two disjoint set d_1 and d_2 satisfies $d_1 \cup d_2 = \{1, 2, \dots, d_z\}$. This transformation is inherently invertible, maintaining the topological properties of the state space.

Each flow model exhibits its own strengths and limitations. The choice of a flow model should be contingent upon the dataset’s nature, the problem’s specific requirements, and computational constraints. Therefore, the selection of a flow model is empirically refined during hyperparameter tuning.

Training algorithm for DualDynamics framework

We present the algorithm for the proposed DualDynamics framework. The presented algorithm 1 concisely captures the training procedure of the DualDynamics framework. Here we showcase the example of proposed method using Neural CDE for classification task with cross-entropy loss.

Algorithm 1: Training Procedure for DualDynamics (using Neural CDE for classification task)

1: Initialized model parameters $\Theta = \{\theta_h, \theta_f, \theta_k, \theta_G, \theta_{MLP}\}$.

2: **Forward Pass:**

3: Compute initial latent state $\mathbf{z}(0) = h(\mathbf{x}_0; \theta_h)$ and solve Neural CDE to obtain $\mathbf{z}(t)$:

$$\mathbf{z}(t) = \mathbf{z}(0) + \int_0^t f(s, \mathbf{z}(s); \theta_f) dX(s)$$

4: Aggregate $\mathbf{z}(t)$ to compute $\hat{\mathbf{z}}(0) = k(\mathbf{z}; \theta_k)$ and compute $\hat{\mathbf{z}}(t)$ using flow model \mathcal{G} :

$$\hat{\mathbf{z}}(t) = \mathcal{G}(t, \hat{\mathbf{z}}(0); \theta_G)$$

5: **Loss Computation:**

6: Compute cross-entropy loss \mathcal{L} using $\hat{\mathbf{z}}(T)$ and target y .

$$\mathcal{L} = - \sum_{i=1}^C y_i \log(\text{softmax}(MLP(\hat{\mathbf{z}}(T); \theta_{MLP}))_i)$$

7: **Backward Pass:**

8: Compute gradients $\nabla_{\theta} \mathcal{L}$ using adjoint-based backpropagation:

$$\frac{\partial \mathcal{L}}{\partial \theta_f} = \int_0^T \lambda_z(t)^\top \frac{\partial f(t, \mathbf{z}(t); \theta_f)}{\partial \theta_f} \frac{dX(t)}{dt} dt, \quad \frac{\partial \mathcal{L}}{\partial \theta_G} = \lambda_z(T)^\top \frac{\partial \mathcal{G}(T, \hat{\mathbf{z}}(0); \theta_G)}{\partial \theta_G}.$$

9: Update all parameters. $\Theta \leftarrow \Theta - \eta \nabla_{\Theta} \mathcal{L}$

Detailed results for “Robust classification with the missing data”

Data preparation

In our study, we conducted classification experiments across 18 diverse datasets, in three distinct domains, from the University of East Anglia (UEA) and the University of California Riverside (UCR) Time Series Classification Repository ⁴ (Bagnall et al. 2018) using the python library `sktime` (Löning et al. 2019). As outlined in Table 7, the datasets in the Sensor domain are univariate, whereas the others encompass a mix of univariate and multivariate data. Addressing the challenge posed by varying lengths of time series, the strategy of uniform scaling was employed to align all series to the dimension of the longest series (Keogh 2003; Yankov et al. 2007; Gao and Lin 2018; Tan et al. 2019). The partitioning of the dataset into training, validation, and testing subsets was executed in proportions of 0.70, 0.15, and 0.15 respectively. Subsequent to this partitioning, a random assortment of missing observations was introduced for each variable. Lastly, these modified variables are integrated into combined dataset.

Table 7: Description of datasets for the classification task

Domain	Dataset	Total number of samples	Number of classes	Dimension of time series	Length of time series
Motion & HAR	BasicMotions	80	4	6	100
	Epilepsy	275	4	3	206
	PickupGestureWiimoteZ	100	10	1	29-361
	ShakeGestureWiimoteZ	100	10	1	41-385
	ToeSegmentation1	268	2	1	277
	ToeSegmentation2	166	2	1	343
ECG & EEG	Blink	950	2	4	510
	ECG200	200	2	1	96
	SelfRegulationSCP1	561	2	6	896
	SelfRegulationSCP2	380	2	7	1152
	StandWalkJump	27	3	4	2500
	TwoLeadECG	1162	2	1	82
Sensor	DodgerLoopDay	158	7	1	288
	DodgerLoopGame	158	2	1	288
	DodgerLoopWeekend	158	2	1	288
	Lightning2	121	2	1	637
	Lightning7	143	7	1	319
	Trace	200	4	1	275

Experimental protocol

We utilized the source codes for `torchcde` library⁵ (Kidger et al. 2020; Morrill et al. 2021), and Neural Flow⁶ (Biloš et al. 2021) for the proposed method. In case of benchmark, we used implementation of RNN, LSTM, and GRU using `pytorch`⁷ (Paszke et al. 2019). Also, this research incorporated the primary Neural CDE algorithms from their original repository⁸ (Kidger et al. 2020), which included methodologies such as GRU- Δt , GRU-D, GRU-ODE, ODE-RNN, and Neural CDE. Further, this study leveraged the primary source code of MTAN⁹ (Shukla and Marlin 2021), MIAM¹⁰ (Lee et al. 2022), ODE-LSTM¹¹ (Lechner and Hasani 2020), Neural RDE¹² (Morrill et al. 2021), ANCDE¹³ (Jhin et al. 2024), EXIT¹⁴ (Jhin et al. 2022), and LEAP¹⁵ (Jhin et al. 2023) for a comprehensive evaluation.

The integrity of the comparative analysis was upheld by utilizing the original architectural designs for all methods. Due to the variability of optimal hyperparameters across different methods and datasets, the `ray` library¹⁶ (Moritz et al. 2018; Liaw et al. 2018) was employed for the refinement of these parameters. This library facilitates the automatic tuning of hyperparameters to minimize validation loss, marking a departure from previous studies that necessitated manual adjustments per dataset and model. Optimal hyperparameters determined for regular time series datasets were also applied to their irregular counterparts. The Euler(-Maruyama) method was consistently used as the ODE solver for all approaches in implicit methods.

⁴<http://www.timeseriesclassification.com/>

⁵<https://github.com/patrick-kidger/torchcde>

⁶<https://github.com/mbilos/neural-flows-experiments>

⁷<https://pytorch.org/>

⁸<https://github.com/patrick-kidger/NeuralCDE>

⁹<https://github.com/reml-lab/mTAN>

¹⁰<https://github.com/ku-milab/MIAM>

¹¹<https://github.com/mlech261/ode-lstms>

¹²<https://github.com/jambo6/neuralRDEs>

¹³<https://github.com/sheoyon-jhin/ANCDE>

¹⁴<https://github.com/sheoyon-jhin/EXIT>

¹⁵<https://github.com/alflsowl12/LEAP>

¹⁶<https://github.com/ray-project/ray>

In each model and dataset, the hyperparameters fine-tuned to minimize validation loss included the number of layers n_l and the dimensions of the hidden vector n_h . For RNN-based methods such as RNN, LSTM, and GRU, these hyperparameters were integral to the fully-connected layer, while for NDE-based approaches, they were pertinent to the embedding layer and vector fields. Hyperparameter optimization was systematically conducted: the learning rate lr was calibrated from 10^{-4} to 10^{-1} via log-uniform search; n_l was set through grid search from the set $\{1, 2, 3, 4\}$; and n_h was determined from the set $\{16, 32, 64, 128\}$ through grid search. The batch size was chosen from the set $\{16, 32, 64, 128\}$, considering the total size of the data. All models underwent a training duration of 100 epochs, with the most effective model being chosen based on the lowest validation loss, thereby ensuring its generalizability.

Motivating example: BasicMotions

Table 8: Performance and computation time using ‘BasicMotions’ dataset under regular (0% missingness) and irregular (30%, 50%, and 70% missingness) scenarios (Computation time is calculated without early-stopping)

Methods		Regular	30% Missing	50% Missing	70% Missing	Average	Computation time (s)
RNN-based	RNN	0.750 ± 0.059	0.633 ± 0.095	0.600 ± 0.070	0.583 ± 0.059	0.642 ± 0.071	2.27 ± 0.06
	LSTM	0.833 ± 0.132	0.833 ± 0.156	0.700 ± 0.095	0.700 ± 0.112	0.767 ± 0.124	2.84 ± 0.93
	GRU	0.950 ± 0.046	0.967 ± 0.075	0.900 ± 0.091	0.883 ± 0.173	0.925 ± 0.096	2.97 ± 0.05
	GRU- Δt	0.950 ± 0.075	1.000 ± 0.000	0.967 ± 0.046	0.950 ± 0.046	0.967 ± 0.041	34.39 ± 0.27
	GRU-D	0.967 ± 0.075	0.950 ± 0.112	0.933 ± 0.070	0.967 ± 0.046	0.954 ± 0.075	42.43 ± 0.29
Attention-based	Transformer	0.983 ± 0.037	0.900 ± 0.109	0.967 ± 0.046	0.933 ± 0.091	0.946 ± 0.071	5.75 ± 0.39
	MTAN	0.950 ± 0.112	0.717 ± 0.247	0.717 ± 0.247	0.700 ± 0.046	0.771 ± 0.163	38.77 ± 0.71
	MIAM	0.967 ± 0.046	0.983 ± 0.037	0.933 ± 0.109	0.867 ± 0.126	0.938 ± 0.079	112.34 ± 1.43
ODE-based	GRU-ODE	1.000 ± 0.000	0.967 ± 0.075	0.983 ± 0.037	0.933 ± 0.070	0.971 ± 0.045	519.78 ± 0.34
	ODE-RNN	0.983 ± 0.037	1.000 ± 0.000	1.000 ± 0.000	1.000 ± 0.000	0.996 ± 0.009	113.29 ± 0.17
	ODE-LSTM	0.733 ± 0.109	0.683 ± 0.037	0.717 ± 0.126	0.567 ± 0.216	0.675 ± 0.122	73.03 ± 0.73
CDE-based	Neural CDE	0.983 ± 0.037	1.000 ± 0.000	0.983 ± 0.037	0.900 ± 0.037	0.967 ± 0.028	112.53 ± 0.41
	Neural RDE	0.983 ± 0.037	0.983 ± 0.037	0.950 ± 0.075	0.833 ± 0.083	0.938 ± 0.058	93.79 ± 0.44
	ANCDE	1.000 ± 0.000	0.967 ± 0.046	0.983 ± 0.037	0.900 ± 0.137	0.963 ± 0.055	360.50 ± 0.47
	EXIT	0.300 ± 0.112	0.450 ± 0.095	0.417 ± 0.102	0.367 ± 0.139	0.383 ± 0.112	334.53 ± 0.28
	LEAP	0.317 ± 0.149	0.300 ± 0.095	0.317 ± 0.124	0.167 ± 0.083	0.275 ± 0.113	163.04 ± 0.59
Flow-based	Neural Flow	0.717 ± 0.139	0.433 ± 0.207	0.433 ± 0.109	0.367 ± 0.126	0.487 ± 0.145	4.64 ± 0.28
Proposed method		1.000 ± 0.000	1.000 ± 0.000	0.983 ± 0.037	0.983 ± 0.037	0.992 ± 0.019	119.08 ± 2.70

Table 8 presents the classification outcomes for both with and without missingness. While Neural CDE generally exhibits robust performance, its extended variants tend to require increased computation time and do not consistently perform well across a broad range of tasks compared to the benchmark performance. On the other hand, Neural Flow achieves rapid convergence with reduced performance. In contrast, our proposed method not only shows superior performance but also maintains a balanced computational demand.

Detailed results of ablation study

Table 9: Ablation study of the proposed method (Values in parentheses show average of 18 standard deviations)

Configuration	Regular		30% Missing		50% Missing		70% Missing	
	Accuracy	Loss	Accuracy	Loss	Accuracy	Loss	Accuracy	Loss
Proposed method (Neural CDE)	0.724 (0.090)	0.631 (0.145)	0.720 (0.088)	0.703 (0.180)	0.691 (0.091)	0.712 (0.173)	0.697 (0.098)	0.698 (0.176)
- Baseline	0.681 (0.073)	0.719 (0.252)	0.672 (0.068)	0.739 (0.253)	0.661 (0.070)	0.768 (0.248)	0.652 (0.091)	0.836 (0.303)
- Conventional MLP	0.592 (0.084)	0.812 (0.143)	0.578 (0.091)	0.870 (0.152)	0.578 (0.087)	0.888 (0.163)	0.582 (0.085)	0.879 (0.136)
- ResNet Flow	0.678 (0.084)	0.714 (0.141)	0.662 (0.094)	0.791 (0.181)	0.638 (0.086)	0.791 (0.160)	0.625 (0.100)	0.812 (0.138)
- GRU Flow	0.669 (0.079)	0.685 (0.135)	0.662 (0.078)	0.776 (0.184)	0.656 (0.074)	0.803 (0.178)	0.652 (0.083)	0.810 (0.191)
- Coupling Flow	0.675 (0.098)	0.715 (0.166)	0.673 (0.090)	0.745 (0.197)	0.667 (0.096)	0.769 (0.185)	0.662 (0.102)	0.758 (0.194)
Proposed method (Neural ODE)	0.540 (0.059)	0.948 (0.064)	0.534 (0.076)	0.971 (0.078)	0.535 (0.064)	0.977 (0.077)	0.531 (0.066)	0.978 (0.070)
- Baseline	0.511 (0.069)	0.973 (0.080)	0.503 (0.072)	0.983 (0.078)	0.489 (0.068)	0.985 (0.084)	0.506 (0.066)	0.982 (0.069)
- Conventional MLP	0.521 (0.062)	0.957 (0.065)	0.503 (0.067)	0.981 (0.082)	0.494 (0.063)	0.993 (0.085)	0.496 (0.071)	0.988 (0.071)
- ResNet Flow	0.528 (0.071)	0.960 (0.062)	0.505 (0.059)	0.978 (0.087)	0.503 (0.051)	0.987 (0.081)	0.504 (0.059)	0.987 (0.076)
- GRU Flow	0.525 (0.057)	0.965 (0.063)	0.530 (0.083)	0.974 (0.083)	0.520 (0.075)	0.999 (0.104)	0.515 (0.068)	0.986 (0.068)
- Coupling Flow	0.532 (0.061)	0.944 (0.064)	0.528 (0.077)	0.976 (0.075)	0.522 (0.057)	0.983 (0.072)	0.509 (0.062)	0.980 (0.068)
Proposed method (Neural SDE)	0.543 (0.066)	0.958 (0.083)	0.531 (0.063)	0.971 (0.063)	0.537 (0.073)	0.974 (0.071)	0.541 (0.061)	0.970 (0.068)
- Baseline	0.521 (0.063)	0.961 (0.073)	0.502 (0.059)	0.977 (0.078)	0.505 (0.057)	0.983 (0.072)	0.507 (0.064)	0.992 (0.069)
- Conventional MLP	0.516 (0.065)	0.961 (0.084)	0.495 (0.070)	0.995 (0.075)	0.511 (0.073)	0.984 (0.074)	0.503 (0.068)	0.983 (0.073)
- ResNet Flow	0.526 (0.066)	0.965 (0.064)	0.518 (0.070)	0.964 (0.075)	0.513 (0.061)	0.972 (0.079)	0.522 (0.060)	0.973 (0.073)
- GRU Flow	0.520 (0.058)	0.980 (0.086)	0.528 (0.069)	0.980 (0.075)	0.522 (0.078)	0.982 (0.063)	0.515 (0.066)	0.984 (0.070)
- Coupling Flow	0.528 (0.071)	0.961 (0.087)	0.513 (0.068)	0.976 (0.076)	0.511 (0.062)	0.983 (0.083)	0.526 (0.071)	0.981 (0.070)

Table 9 presents a comprehensive ablation study of our DualDynamics framework, comparing various combinations of implicit components (Neural ODE, CDE, and SDE) and explicit components (ResNet Flow, GRU Flow, and

Coupling Flow) against a non-invertible conventional MLP baseline. Neural CDEs consistently outperform Neural ODEs and SDEs, aligning with previous findings in the literature. While the optimal flow configuration varies across datasets, all flow models demonstrate superior performance compared to the MLP baseline. This consistent improvement underscores the efficacy of our framework’s synergistic integration of implicit and explicit components.

Variations in model architecture

Our framework’s architecture allows for several potential variations, each with distinct trade-offs. In this section, we compare the versatility of our framework with two potential perspectives. One possible modification is to utilize only $\mathbf{z}(t)$ instead of $\hat{\mathbf{z}}(t)$ after training the unified framework. However, this approach would significantly limit the model’s expressiveness, as it fails to leverage the unique properties of the flow model, particularly its ability to model complex probability distributions through invertible transformations, as shown in Table 10.

Table 10: Comparative study of latent value selection

Configuration	Regular		30% Missing		50% Missing		70% Missing	
	Accuracy	Loss	Accuracy	Loss	Accuracy	Loss	Accuracy	Loss
Proposed method (Neural CDE)	1.000 (0.000)	0.007 (0.008)	1.000 (0.000)	0.021 (0.027)	0.983 (0.037)	0.044 (0.063)	0.983 (0.037)	0.069 (0.141)
- using $\mathbf{z}(t)$ instead	1.000 (0.000)	0.152 (0.087)	1.000 (0.000)	0.144 (0.119)	1.000 (0.000)	0.126 (0.126)	0.883 (0.095)	0.346 (0.174)
Neural CDE	0.983 (0.037)	0.037 (0.056)	1.000 (0.000)	0.048 (0.043)	0.983 (0.037)	0.071 (0.061)	0.900 (0.037)	0.433 (0.242)
Neural Flow	0.717 (0.139)	0.969 (0.340)	0.433 (0.207)	1.384 (0.285)	0.433 (0.109)	1.382 (0.382)	0.367 (0.126)	1.521 (0.343)

Another consideration is the replacement of the flow model with more sophisticated architectures such as feedforward networks (Hornik, Stinchcombe, and White 1989), gated recurrent unit (Chung et al. 2014), temporal convolution networks (Lea et al. 2017), or transformer-based attention mechanisms (Vaswani et al. 2017). Table 11 summarizes the analysis of different model components in our framework. While these alternatives demonstrate strong performance on regularly-sampled time series, they often struggle with irregular sampling patterns and missing data. Compared to that, the flow model in our current architecture specifically addresses these challenges.

Table 11: Comparative study of component selection

Configuration	Regular		30% Missing		50% Missing		70% Missing	
	Accuracy	Loss	Accuracy	Loss	Accuracy	Loss	Accuracy	Loss
Proposed method (Neural CDE)	1.000 (0.000)	0.007 (0.008)	1.000 (0.000)	0.021 (0.027)	0.983 (0.037)	0.044 (0.063)	0.983 (0.037)	0.069 (0.141)
- Conventional MLP	0.950 (0.075)	0.131 (0.104)	0.933 (0.037)	0.263 (0.179)	0.950 (0.046)	0.167 (0.113)	0.933 (0.037)	0.214 (0.053)
- Feedforward network	1.000 (0.000)	0.023 (0.014)	0.983 (0.037)	0.066 (0.042)	0.900 (0.109)	0.314 (0.278)	0.850 (0.070)	0.432 (0.152)
- Gated recurrent unit	0.983 (0.037)	0.050 (0.063)	0.883 (0.075)	0.402 (0.339)	0.883 (0.046)	0.333 (0.176)	0.867 (0.075)	0.450 (0.199)
- Temporal convolution	0.850 (0.149)	0.386 (0.298)	0.850 (0.091)	0.455 (0.383)	0.900 (0.070)	0.408 (0.211)	0.767 (0.109)	0.575 (0.272)
- Transformer	0.917 (0.083)	0.254 (0.252)	0.950 (0.112)	0.292 (0.639)	0.950 (0.075)	0.195 (0.286)	0.867 (0.095)	0.521 (0.390)

Detailed results three domains

Our investigation involved 18 datasets classified into three domains. We collate the outcomes across three domains: Motion & HAR, ECG & EEG, and Sensor datasets, in Tables 12, 13, and 14. We observe variability in the performance metrics due to the unique characteristics of each domain. Figure 7 shows the strong interdependence between the efficacy of our proposed approach and the distinctive attributes of the datasets under examination. In summary, the proposed methodology demonstrates superior performance relative to benchmark models.

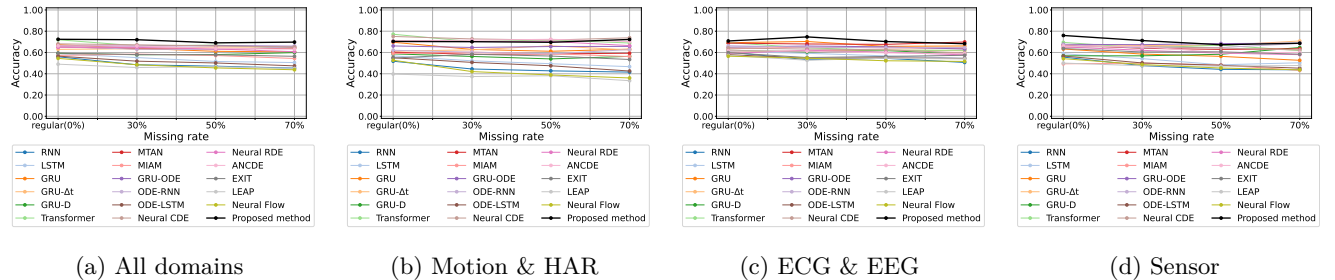


Figure 7: Comparison of performance across diverse domains and four missing rate scenarios

Table 12: Average classification performance on 6 datasets in Motion & HAR

Methods	Regular		30% Missing		50% Missing		70% Missing		Average	
	Accuracy	Rank	Accuracy	Rank	Accuracy	Rank	Accuracy	Rank	Accuracy	Rank
RNN	0.518 (0.062)	13.3	0.445 (0.077)	15.8	0.427 (0.061)	15.6	0.415 (0.070)	14.5	0.451 (0.067)	14.8
LSTM	0.568 (0.089)	11.6	0.522 (0.092)	11.9	0.494 (0.094)	12.3	0.467 (0.090)	13.3	0.513 (0.091)	12.3
GRU	0.696 (0.095)	7.2	0.629 (0.076)	10.3	0.612 (0.089)	9.6	0.631 (0.111)	7.8	0.642 (0.093)	8.7
GRU-Δt	0.613 (0.076)	9.3	0.624 (0.079)	7.6	0.663 (0.064)	7.3	0.624 (0.077)	9.3	0.631 (0.074)	8.4
GRU-D	0.587 (0.077)	11.6	0.563 (0.089)	11.3	0.540 (0.056)	13.2	0.564 (0.054)	11.2	0.563 (0.069)	11.8
Transformer	0.772 (0.060)	3.2	0.703 (0.070)	4.8	0.718 (0.079)	4.3	0.689 (0.069)	4.3	0.720 (0.070)	4.1
MIAM	0.603 (0.096)	12.7	0.583 (0.116)	9.9	0.587 (0.099)	9.2	0.593 (0.063)	9.2	0.591 (0.093)	10.2
MIAM	0.590 (0.091)	9.0	0.603 (0.063)	7.8	0.589 (0.066)	8.6	0.562 (0.044)	9.8	0.586 (0.066)	8.8
GRU-ODE	0.662 (0.081)	8.8	0.647 (0.091)	9.5	0.656 (0.072)	8.7	0.657 (0.084)	7.0	0.656 (0.082)	8.5
ODE-RNN	0.621 (0.087)	9.8	0.603 (0.078)	8.6	0.588 (0.095)	8.8	0.627 (0.064)	7.6	0.610 (0.081)	8.7
ODE-LSTM	0.550 (0.083)	12.8	0.507 (0.080)	12.8	0.475 (0.102)	13.7	0.426 (0.094)	13.2	0.489 (0.089)	13.1
Neural CDE	0.751 (0.096)	5.9	0.728 (0.080)	5.5	0.717 (0.100)	5.9	0.738 (0.111)	6.2	0.733 (0.097)	5.9
Neural RDE	0.702 (0.091)	6.2	0.703 (0.077)	6.1	0.704 (0.088)	6.5	0.665 (0.095)	7.6	0.693 (0.088)	6.6
ANCDE	0.710 (0.068)	5.8	0.716 (0.075)	5.0	0.724 (0.074)	4.1	0.703 (0.077)	5.5	0.713 (0.074)	5.1
EXIT	0.548 (0.086)	10.8	0.584 (0.073)	9.3	0.567 (0.086)	10.4	0.534 (0.086)	11.8	0.558 (0.086)	10.6
LEAP	0.397 (0.084)	15.7	0.374 (0.086)	16.0	0.381 (0.077)	14.1	0.335 (0.062)	14.8	0.372 (0.077)	15.1
Neural Flow	0.527 (0.068)	11.3	0.420 (0.081)	13.3	0.389 (0.084)	14.1	0.360 (0.065)	14.3	0.424 (0.074)	13.2
Proposed method	0.704 (0.082)	6.3	0.702 (0.074)	5.6	0.696 (0.088)	4.9	0.723 (0.123)	3.7	0.706 (0.092)	5.1

Table 13: Average classification performance on 6 datasets in ECG & EEG

Methods	Regular		30% Missing		50% Missing		70% Missing		Average	
	Accuracy	Rank	Accuracy	Rank	Accuracy	Rank	Accuracy	Rank	Accuracy	Rank
RNN	0.604 (0.075)	10.1	0.532 (0.058)	14.2	0.545 (0.062)	11.8	0.506 (0.056)	14.2	0.547 (0.063)	12.6
LSTM	0.609 (0.054)	10.8	0.592 (0.066)	8.5	0.568 (0.057)	9.7	0.546 (0.048)	10.1	0.579 (0.056)	9.8
GRU	0.692 (0.073)	5.8	0.704 (0.050)	5.2	0.658 (0.068)	7.9	0.661 (0.068)	6.9	0.679 (0.067)	6.5
GRU-Δt	0.602 (0.047)	12.6	0.616 (0.052)	10.7	0.624 (0.062)	8.5	0.616 (0.069)	9.8	0.614 (0.057)	10.4
GRU-D	0.621 (0.056)	10.0	0.606 (0.066)	11.0	0.618 (0.055)	9.8	0.585 (0.061)	12.3	0.608 (0.060)	10.8
Transformer	0.693 (0.067)	8.9	0.643 (0.056)	10.2	0.621 (0.066)	10.8	0.621 (0.088)	11.1	0.645 (0.069)	10.3
MIAM	0.688 (0.081)	8.2	0.680 (0.115)	5.8	0.676 (0.093)	4.9	0.699 (0.093)	4.8	0.686 (0.096)	5.9
GRU-ODE	0.634 (0.062)	11.3	0.651 (0.063)	7.9	0.644 (0.055)	7.2	0.637 (0.058)	7.8	0.642 (0.060)	8.5
GRU-RNN	0.650 (0.057)	8.1	0.661 (0.057)	6.8	0.653 (0.063)	7.5	0.633 (0.080)	8.4	0.649 (0.064)	7.7
ODE-LSTM	0.664 (0.068)	6.3	0.650 (0.050)	7.4	0.644 (0.048)	9.0	0.647 (0.050)	6.2	0.651 (0.054)	7.2
ODE-LSTM	0.580 (0.068)	9.6	0.546 (0.065)	12.3	0.550 (0.054)	12.8	0.545 (0.036)	12.8	0.555 (0.053)	11.8
Neural CDE	0.643 (0.040)	8.1	0.632 (0.038)	8.3	0.625 (0.041)	8.8	0.596 (0.063)	8.3	0.624 (0.047)	8.3
Neural RDE	0.591 (0.065)	12.5	0.621 (0.060)	8.6	0.602 (0.070)	9.3	0.577 (0.073)	9.3	0.598 (0.067)	9.9
ANCDE	0.617 (0.075)	9.3	0.612 (0.060)	9.3	0.596 (0.059)	11.3	0.590 (0.072)	7.9	0.604 (0.066)	9.4
EXIT	0.599 (0.092)	10.8	0.552 (0.084)	12.8	0.563 (0.092)	11.2	0.574 (0.044)	10.2	0.572 (0.078)	11.2
LEAP	0.572 (0.051)	12.3	0.527 (0.080)	14.3	0.546 (0.093)	11.8	0.540 (0.086)	12.5	0.546 (0.077)	12.7
Neural Flow	0.565 (0.047)	11.7	0.547 (0.053)	12.4	0.522 (0.046)	13.3	0.516 (0.047)	12.4	0.538 (0.048)	12.5
Proposed method	0.708 (0.119)	4.8	0.747 (0.086)	5.5	0.703 (0.086)	6.3	0.683 (0.096)	6.3	0.710 (0.097)	5.5

Table 14: Average classification performance on 6 datasets in Sensor

Methods	Regular		30% Missing		50% Missing		70% Missing		Average	
	Accuracy	Rank	Accuracy	Rank	Accuracy	Rank	Accuracy	Rank	Accuracy	Rank
RNN	0.557 (0.078)	12.4	0.476 (0.089)	14.1	0.441 (0.123)	14.7	0.437 (0.079)	14.6	0.478 (0.092)	13.9
LSTM	0.588 (0.059)	10.5	0.542 (0.067)	10.2	0.484 (0.069)	12.3	0.503 (0.065)	10.4	0.529 (0.065)	10.8
GRU	0.633 (0.073)	9.0	0.585 (0.072)	9.7	0.563 (0.059)	9.5	0.526 (0.084)	11.0	0.577 (0.072)	9.8
GRU-Δt	0.673 (0.072)	7.9	0.666 (0.075)	6.3	0.668 (0.080)	5.8	0.708 (0.075)	4.4	0.679 (0.076)	6.1
GRU-D	0.569 (0.130)	11.1	0.569 (0.105)	9.5	0.583 (0.115)	8.8	0.647 (0.070)	7.0	0.592 (0.105)	9.1
Transformer	0.695 (0.068)	8.3	0.643 (0.073)	9.2	0.669 (0.081)	7.1	0.618 (0.079)	9.3	0.656 (0.074)	8.4
MIAM	0.671 (0.088)	7.3	0.639 (0.063)	6.4	0.629 (0.074)	6.3	0.635 (0.063)	6.6	0.643 (0.072)	6.6
MIAM	0.493 (0.085)	15.3	0.500 (0.132)	14.2	0.482 (0.093)	14.1	0.432 (0.086)	15.5	0.477 (0.099)	14.8
GRU-ODE	0.677 (0.079)	6.0	0.674 (0.059)	5.8	0.684 (0.072)	4.3	0.687 (0.079)	5.2	0.680 (0.072)	5.3
ODE-RNN	0.673 (0.098)	5.9	0.642 (0.101)	7.3	0.647 (0.115)	5.7	0.684 (0.062)	5.8	0.662 (0.094)	6.2
ODE-LSTM	0.567 (0.083)	11.8	0.502 (0.061)	13.0	0.479 (0.049)	13.5	0.453 (0.075)	14.3	0.500 (0.067)	13.1
Neural CDE	0.650 (0.082)	8.8	0.657 (0.087)	8.4	0.641 (0.069)	7.3	0.623 (0.094)	7.3	0.643 (0.083)	8.0
Neural RDE	0.653 (0.089)	7.0	0.620 (0.076)	7.7	0.594 (0.077)	8.0	0.580 (0.069)	8.7	0.612 (0.078)	8.0
ANCDE	0.660 (0.106)	8.8	0.656 (0.115)	6.8	0.598 (0.108)	9.3	0.601 (0.069)	8.6	0.629 (0.100)	8.4
EXIT	0.637 (0.082)	8.7	0.605 (0.107)	9.5	0.606 (0.081)	8.6	0.584 (0.074)	9.2	0.608 (0.086)	9.0
LEAP	0.500 (0.052)	15.3	0.475 (0.044)	14.8	0.471 (0.054)	14.9	0.478 (0.073)	13.8	0.481 (0.056)	14.7
Neural Flow	0.542 (0.063)	12.8	0.487 (0.067)	14.5	0.454 (0.043)	15.5	0.437 (0.049)	15.5	0.480 (0.055)	14.6
Proposed method	0.760 (0.070)	4.3	0.712 (0.106)	3.8	0.673 (0.100)	4.9	0.687 (0.076)	3.9	0.708 (0.088)	4.2

Detailed results for “Interpolation for the missing data”

The interpolation experiment was conducted using the 2012 PhysioNet Mortality dataset (Silva et al. 2012), which comprises multivariate time series data from ICU records. This dataset includes 37 variables collected from Intensive Care Unit (ICU) records, with each data instance capturing sporadic and infrequent measurements obtained within the initial 48-hour window post-admission to the ICU. Following the methodologies proposed by Rubanova, Chen, and Duvenaud (2019), we adjusted the observation timestamps to the nearest minute, thereby creating up to 2880 possible measurement intervals per time series. Our experiments adhered to the methodology proposed by Shukla and Marlin (2021), involving the alteration of observation frequency from 50% to 90% to predict the remaining data.

We followed experimental protocol suggested by Shukla and Marlin (2021), and its Github repository¹⁷. For the proposed methodology, the training process spans 300 epochs, employing a batch size of 64 and a learning rate of 0.001. To train our models on a dataset comprising irregularly sampled time series, we adopt a strategy from Shukla and Marlin (2021). This involves the modified VAE training method, where we optimize a normalized variational lower bound of the log marginal likelihood, grounded on the evidence lower bound (ELBO).

Table 15 presents an ablation study on the interpolation task. Our DualDynamics framework significantly improves interpolation performance, with flow model architectures consistently outperforming conventional MLPs in terms of MSE. This performance gap, observed even with comparable network capacities, underscores the importance of our framework’s architectural design over mere network size in enhancing interpolation accuracy for time series data.

Table 15: Ablation study on the PhysioNet Mortality Dataset MSE $\times 10^{-3}$

Configuration	Test MSE $\times 10^{-3}$				
	50%	60%	70%	80%	90%
Conventional MLP	3.838 \pm 0.021	3.655 \pm 0.016	3.508 \pm 0.010	3.316 \pm 0.062	3.442 \pm 0.078
ResNet Flow	3.655 \pm 0.031	3.537 \pm 0.020	3.373 \pm 0.042	3.351 \pm 0.154	3.171 \pm 0.057
GRU Flow	3.754 \pm 0.014	3.562 \pm 0.019	3.470 \pm 0.031	3.232 \pm 0.101	3.222 \pm 0.030
Coupling Flow	3.631 \pm 0.049	3.659 \pm 0.028	3.463 \pm 0.032	3.224 \pm 0.044	3.114 \pm 0.050

The optimal hyperparameters for the proposed methods are remarked in bold within Table 16, encompassing observed data with 50%. We used the same hyperparameters to the remainder settings of 60%, 70%, 80%, and 90%.

Table 16: Results of hyperparameter tuning for PhysioNet Mortality Dataset (MSE $\times 10^{-3}$)

n_l	n_h	Conventional MLP	ResNet Flow	GRU Flow	Coupling Flow
1	16	4.574 \pm 0.072	4.534 \pm 0.041	4.753 \pm 0.068	4.473 \pm 0.159
	32	4.332 \pm 0.121	4.134 \pm 0.014	4.241 \pm 0.058	4.302 \pm 0.074
	64	3.991 \pm 0.053	4.370 \pm 0.062	3.901 \pm 0.075	4.276 \pm 0.145
	128	3.839 \pm 0.064	4.072 \pm 0.042	4.097 \pm 0.053	4.118 \pm 0.083
2	16	4.593 \pm 0.102	4.692 \pm 0.032	4.685 \pm 0.102	4.560 \pm 0.056
	32	4.253 \pm 0.046	4.208 \pm 0.104	4.540 \pm 0.053	4.519 \pm 0.106
	64	4.459 \pm 0.069	4.006 \pm 0.062	4.104 \pm 0.109	3.983 \pm 0.047
	128	3.876 \pm 0.026	4.355 \pm 0.043	3.778 \pm 0.045	3.871 \pm 0.037
3	16	4.580 \pm 0.088	4.475 \pm 0.116	4.866 \pm 0.054	4.635 \pm 0.129
	32	4.332 \pm 0.010	4.096 \pm 0.111	4.253 \pm 0.028	4.146 \pm 0.030
	64	3.997 \pm 0.115	4.035 \pm 0.153	4.185 \pm 0.106	4.048 \pm 0.119
	128	3.838 \pm 0.021	3.655 \pm 0.031	3.754 \pm 0.014	3.631 \pm 0.049
4	16	4.552 \pm 0.070	4.472 \pm 0.077	4.744 \pm 0.021	4.554 \pm 0.067
	32	4.312 \pm 0.044	4.237 \pm 0.054	4.696 \pm 0.185	4.221 \pm 0.065
	64	4.082 \pm 0.036	3.995 \pm 0.023	4.175 \pm 0.052	3.955 \pm 0.054
	128	3.848 \pm 0.048	3.950 \pm 0.042	3.982 \pm 0.117	4.328 \pm 0.048

Detailed results for “Classification of irregularly-sampled data”

We utilized the PhysioNet Sepsis dataset (Reyna et al. 2019) to investigate classification performance with irregularly-sampled time series. The dataset comprises 40,335 patient instances from ICU, characterized by 34 temporal variables such as heart rate, oxygen saturation, and body temperature.

Given that the PhysioNet dataset represents irregular time series, with only 10% of the data points timestamped for each patient, the study addresses this irregularity through two distinct approaches to time-series classification as suggested by Kidger et al. (2020): (i) classification utilizing observation intensity (OI) and (ii) classification without utilizing observation intensity (No OI). Observation intensity serves as an indicator of the severity of a patient’s condition, and when employed, each data point in the time series is supplemented with an index reflecting this intensity. Considering the dataset’s skewed distribution, performance is evaluated using the Area Under the Receiver Operating Characteristic Curve (AUROC) metric. Benchmark performance is established in Jhin et al. (2022).

¹⁷<https://github.com/reml-lab/mTAN>

Table 17: Ablation study on PhysioNet Sepsis dataset

Configuration	Test AUROC		Memory (MB)	
	OI	No OI	OI	No OI
Conventional MLP	0.912 ± 0.011	0.861 ± 0.016	284	135
ResNet Flow	0.915 ± 0.003	0.875 ± 0.006	230	156
GRU Flow	0.916 ± 0.003	0.875 ± 0.004	355	178
Coupling Flow	0.918 ± 0.003	0.873 ± 0.004	453	233

We followed experimental protocol suggested by Kidger et al. (2020), and its Github repository¹⁸. For the benchmark methods, we used the reported performance in Jhin et al. (2022). Table 17 presents a comprehensive ablation study comparing various flow configurations integrated with Neural CDEs. We train for 200 epochs with a batch size of 1024 and a learning rate of 0.001. The best hyperparameters are highlighted with bold font in Table 20 and 21.

Detailed results for “Forecasting with the partial observations”

For the **MuJoCo** dataset, we followed experimental protocol suggested by in Jhin et al. (2023) and Jhin et al. (2024). We used reported performance of benchmark methods and source code from the Github repositories¹⁹. For the **Google** dataset, We followed experimental protocol and reported performance established by Jhin et al. (2022). Source code from its Github repository²⁰ was utilized to conduct experiment. We conducted hyperparameter tuning for regular data and the same set of hyperparameters was applied to the scenarios with missingness.

MuJoCo. The Multi-Joint dynamics with Contact (MuJoCo) dataset, developed by Todorov, Erez, and Tassa (2012), is based on the Hopper configuration in the DeepMind control suite (Tassa et al. 2018). This dataset comprises 10,000 simulations, each represented as a 14-dimensional time series with 100 data points sampled at regular intervals. In our experimental protocol, the initial 50 data points in each time series were used to predict the subsequent 10 data points. To introduce complexity and simulate diverse conditions, we systematically excluded a proportion of the data points—30%, 50%, and 70%—from each time series, as detailed in Jhin et al. (2023) and Jhin et al. (2024).

Table 18: Forecasting performance and memory usage on MuJoCo dataset

Configuration	Test MSE				Memory (MB)
	Regular	30% dropped	50% dropped	70% dropped	
Conventional MLP	0.008 ± 0.002	0.009 ± 0.001	0.009 ± 0.001	0.009 ± 0.001	138
ResNet Flow	0.008 ± 0.003	0.008 ± 0.001	0.008 ± 0.001	0.008 ± 0.001	198
GRU Flow	0.006 ± 0.001	0.008 ± 0.001	0.008 ± 0.001	0.008 ± 0.001	318
Coupling Flow	<u>0.008 ± 0.001</u>	0.008 ± 0.001	0.008 ± 0.001	0.008 ± 0.001	409

Table 18 summarize the ablation study of the proposed method on MuJoCo dataset. In the proposed method, the training spanned 500 epochs, with a batch size configured at 1024 and a learning rate set to 0.001. The hyperparameters that were identified as optimal are conspicuously presented in bold within Table 22.

Google. The Google stock data (Jhin et al. 2022) includes transaction volumes of Google, along with metrics such as high, low, open, close, and adjusted closing prices. This dataset spans from 2011 to 2021, and the objective is to utilize historical time-series data from the preceding 50 days to forecast the high, low, open, close, and adjusted closing prices for the next 10-day period. We followed the experimental protocol and reported performances of benchmark methods from Jhin et al. (2022). Similarly to the previous experiment, we excluded partial observations in data.

Table 19: Forecasting performance and memory usage on Google dataset

Configuration	Test MSE				Memory (MB)
	Regular	30% dropped	50% dropped	70% dropped	
Conventional MLP	0.0012 ± 0.0001	0.0011 ± 0.0001	0.0011 ± 0.0001	0.0014 ± 0.0001	52
ResNet Flow	0.0011 ± 0.0001	0.0010 ± 0.0001	0.0011 ± 0.0001	0.0013 ± 0.0001	62
GRU Flow	0.0012 ± 0.0001	0.0010 ± 0.0001	0.0011 ± 0.0001	0.0013 ± 0.0001	81
Coupling Flow	0.0010 ± 0.0001	0.0010 ± 0.0001	0.0009 ± 0.0001	0.0013 ± 0.0002	119

Table 19 summarize the ablation study of the proposed method on Google dataset. In the proposed method, the training spanned 200 epochs, with a batch size configured at 64 and a learning rate set to 0.001. Through grid search, the optimal hyperparameters are highlighted in bold within Table 23.

¹⁸<https://github.com/patrick-kidger/NeuralCDE>

¹⁹<https://github.com/alfsowl12/LEAP>

²⁰<https://github.com/sheoyon-jhin/EXIT>

Table 20: Results of hyperparameter tuning for PhysioNet Sepsis Dataset with observation intensity
(Memory usage in MB, and the number of parameter in $\times 10^3$ unit.)

n_l	n_h	Conventional MLP			ResNet Flow			GRU Flow			Coupling Flow		
		Test AUROC	Memory	# Params	Test AUROC	Memory	# Params	Test AUROC	Memory	# Params	Test AUROC	Memory	# Params
1	16	0.803 ± 0.018	225	23.81	0.867 ± 0.008	225	23.84	0.870 ± 0.014	225	24.15	0.887 ± 0.005	225	24.13
	32	0.851 ± 0.004	227	83.46	0.878 ± 0.003	227	83.52	0.878 ± 0.003	252	84.64	0.880 ± 0.006	286	84.61
	64	0.872 ± 0.004	242	313.35	0.889 ± 0.001	270	313.47	0.887 ± 0.005	355	317.76	0.883 ± 0.004	424	317.70
2	128	0.872 ± 0.002	345	1215.49	0.889 ± 0.006	401	1215.75	0.885 ± 0.004	571	1232.51	0.887 ± 0.005	710	1232.39
	16	0.870 ± 0.010	225	24.35	0.900 ± 0.005	225	24.39	0.895 ± 0.003	225	24.42	0.893 ± 0.003	225	24.67
	32	0.894 ± 0.003	227	85.57	0.901 ± 0.003	227	85.63	0.898 ± 0.003	252	85.70	0.903 ± 0.006	293	86.72
3	64	0.897 ± 0.005	256	321.67	0.905 ± 0.006	284	321.79	0.906 ± 0.003	355	321.92	0.900 ± 0.004	439	326.02
	128	0.881 ± 0.005	373	1248.51	0.894 ± 0.002	430	1248.77	0.896 ± 0.005	571	1249.03	0.895 ± 0.005	738	1265.41
	16	0.892 ± 0.004	225	24.90	0.905 ± 0.006	225	24.93	0.905 ± 0.004	225	24.69	0.905 ± 0.003	225	25.22
4	32	0.904 ± 0.005	227	87.68	0.912 ± 0.003	227	87.75	0.913 ± 0.004	252	86.75	0.916 ± 0.002	300	88.83
	64	0.907 ± 0.005	270	329.99	0.912 ± 0.002	299	330.11	0.913 ± 0.002	355	326.08	0.918 ± 0.003	453	334.34
	128	0.881 ± 0.002	401	1281.54	0.912 ± 0.004	458	1281.79	0.908 ± 0.002	570	1265.54	0.903 ± 0.006	766	1298.43
4	16	0.877 ± 0.007	225	25.44	0.906 ± 0.008	225	25.47	0.907 ± 0.004	225	24.96	0.911 ± 0.005	229	25.76
	32	0.907 ± 0.003	227	89.79	0.915 ± 0.003	230	89.86	0.914 ± 0.002	252	87.81	0.915 ± 0.003	308	90.95
	64	0.912 ± 0.011	284	338.31	0.910 ± 0.004	313	338.43	0.916 ± 0.003	355	330.24	0.911 ± 0.004	467	342.66
128	0.891 ± 0.003	429	1314.56	0.909 ± 0.005	487	1314.82	0.912 ± 0.004	571	1282.05	0.904 ± 0.005	795	1331.46	

Table 21: Results of hyperparameter tuning for PhysioNet Sepsis Dataset without observation intensity
(Memory usage in MB, and the number of parameter in $\times 10^3$ unit.)

n_l	n_h	Conventional MLP			ResNet Flow			GRU Flow			Coupling Flow		
		Test AUROC	Memory	# Params	Test AUROC	Memory	# Params	Test AUROC	Memory	# Params	Test AUROC	Memory	# Params
1	16	0.777 ± 0.018	114	13.76	0.826 ± 0.007	114	13.79	0.827 ± 0.007	128	14.10	0.838 ± 0.008	145	14.08
	32	0.815 ± 0.007	121	46.21	0.838 ± 0.008	135	46.27	0.845 ± 0.006	178	47.39	0.841 ± 0.007	212	47.36
	64	0.815 ± 0.003	165	169.47	0.828 ± 0.004	193	169.60	0.841 ± 0.006	278	173.89	0.833 ± 0.003	348	173.83
2	128	0.790 ± 0.018	259	649.47	0.834 ± 0.004	316	649.73	0.825 ± 0.008	485	666.50	0.837 ± 0.010	624	666.37
	16	0.835 ± 0.005	114	14.31	0.861 ± 0.005	114	14.34	0.860 ± 0.004	128	14.37	0.861 ± 0.004	148	14.63
	32	0.839 ± 0.008	128	48.32	0.860 ± 0.004	142	48.39	0.862 ± 0.006	178	48.45	0.866 ± 0.001	219	49.47
3	64	0.830 ± 0.004	179	177.79	0.856 ± 0.005	208	177.92	0.851 ± 0.006	278	178.05	0.861 ± 0.003	362	182.15
	128	0.820 ± 0.007	287	682.50	0.833 ± 0.008	344	682.75	0.848 ± 0.013	486	683.01	0.845 ± 0.008	653	699.39
	16	0.824 ± 0.018	114	14.85	0.860 ± 0.008	114	14.88	0.865 ± 0.011	128	14.64	0.867 ± 0.007	152	15.17
4	32	0.861 ± 0.016	135	50.43	0.871 ± 0.006	149	50.50	0.875 ± 0.004	178	49.51	0.869 ± 0.004	226	51.59
	64	0.844 ± 0.006	193	186.11	0.859 ± 0.010	222	186.24	0.869 ± 0.003	278	182.21	0.865 ± 0.008	376	190.47
	128	0.818 ± 0.013	316	715.52	0.852 ± 0.006	373	715.78	0.858 ± 0.008	486	699.52	0.856 ± 0.010	681	732.42
4	16	0.799 ± 0.070	114	15.39	0.853 ± 0.010	117	15.43	0.854 ± 0.007	128	14.91	0.871 ± 0.009	155	15.71
	32	0.848 ± 0.017	142	52.55	0.875 ± 0.006	156	52.61	0.867 ± 0.006	178	50.56	0.873 ± 0.004	233	53.70
	64	0.845 ± 0.015	208	194.43	0.863 ± 0.006	236	194.56	0.863 ± 0.006	278	186.37	0.864 ± 0.005	390	198.79
128	0.823 ± 0.004	345	748.55	0.846 ± 0.005	402	748.80	0.858 ± 0.011	486	716.03	0.858 ± 0.010	710	765.44	

Table 22: Results of hyperparameter tuning for MuJoCo Dataset
(Memory usage in MB, and the number of parameter in $\times 10^3$ unit.)

n_l	n_h	Conventional MLP			ResNet Flow			GRU Flow			Coupling Flow		
		Test MSE	Memory	# Params	Test MSE	Memory	# Params	Test MSE	Memory	# Params	Test MSE	Memory	# Params
1	16	0.020 ± 0.001	36	5.10	0.018 ± 0.001	42	5.13	0.017 ± 0.002	57	5.44	0.016 ± 0.002	69	5.42
	32	0.012 ± 0.001	49	18.89	0.012 ± 0.003	62	18.96	0.009 ± 0.001	92	20.08	0.011 ± 0.000	118	20.05
	64	0.009 ± 0.002	77	72.59	0.009 ± 0.003	105	72.72	0.006 ± 0.001	165	77.01	0.008 ± 0.000	214	76.94
	128	0.008 ± 0.001	138	284.43	0.008 ± 0.002	198	284.69	0.006 ± 0.000	318	301.45	0.008 ± 0.002	409	301.33
2	16	0.022 ± 0.002	38	5.65	0.020 ± 0.001	45	5.68	0.017 ± 0.003	57	5.71	0.019 ± 0.002	72	5.97
	32	0.016 ± 0.003	54	21.01	0.013 ± 0.002	67	21.07	0.010 ± 0.001	92	21.13	0.012 ± 0.002	123	22.16
	64	0.012 ± 0.001	87	80.91	0.010 ± 0.002	114	81.04	0.010 ± 0.001	165	81.17	0.011 ± 0.001	225	85.26
	128	0.011 ± 0.001	158	317.45	0.010 ± 0.001	219	317.71	0.008 ± 0.001	319	317.97	0.010 ± 0.000	430	334.35
3	16	0.039 ± 0.021	41	6.19	0.021 ± 0.005	47	6.22	0.016 ± 0.003	57	5.98	0.016 ± 0.004	74	6.51
	32	0.033 ± 0.026	59	23.12	0.014 ± 0.002	72	23.18	0.011 ± 0.002	92	22.19	0.012 ± 0.001	128	24.27
	64	0.032 ± 0.027	97	89.23	0.011 ± 0.000	125	89.36	0.010 ± 0.002	165	85.33	0.010 ± 0.001	234	93.58
	128	0.013 ± 0.004	179	350.48	0.011 ± 0.002	239	350.73	0.008 ± 0.000	319	334.48	0.011 ± 0.001	450	367.37
4	16	0.042 ± 0.018	43	6.73	0.024 ± 0.004	50	6.77	0.022 ± 0.009	57	6.25	0.022 ± 0.006	77	7.05
	32	0.034 ± 0.026	64	25.23	0.014 ± 0.001	78	25.29	0.014 ± 0.003	92	23.25	0.012 ± 0.003	132	26.38
	64	0.032 ± 0.027	107	97.55	0.012 ± 0.002	134	97.68	0.011 ± 0.002	165	89.49	0.009 ± 0.002	245	101.90
	128	0.031 ± 0.028	199	383.50	0.011 ± 0.002	260	383.76	0.008 ± 0.001	319	350.99	0.010 ± 0.000	471	400.40

Table 23: Results of hyperparameter tuning for Google Dataset
(Memory usage in MB, and the number of parameter in $\times 10^3$ unit.)

n_l	n_h	Conventional MLP			ResNet Flow			GRU Flow			Coupling Flow		
		Test MSE	Memory	# Params	Test MSE	Memory	# Params	Test MSE	Memory	# Params	Test MSE	Memory	# Params
1	16	0.0017 ± 0.0001	6	2.97	0.0019 ± 0.0005	8	3.00	0.0017 ± 0.0004	12	3.30	0.0012 ± 0.0000	15	3.29
	32	0.0014 ± 0.0000	10	11.05	0.0013 ± 0.0001	13	11.11	0.0014 ± 0.0001	21	12.23	0.0011 ± 0.0000	26	12.20
	64	0.0013 ± 0.0000	17	42.57	0.0012 ± 0.0000	24	42.70	0.0012 ± 0.0000	40	46.98	0.0011 ± 0.0001	51	46.92
	128	0.0013 ± 0.0000	35	167.05	0.0012 ± 0.0001	51	167.30	0.0012 ± 0.0000	81	184.07	0.0011 ± 0.0001	102	183.94
2	16	0.0015 ± 0.0001	7	3.51	0.0022 ± 0.0009	8	3.54	0.0017 ± 0.0004	12	3.58	0.0011 ± 0.0001	15	3.83
	32	0.0014 ± 0.0000	11	13.16	0.0014 ± 0.0003	14	13.22	0.0014 ± 0.0001	21	13.29	0.0011 ± 0.0000	28	14.31
	64	0.0013 ± 0.0000	19	50.89	0.0012 ± 0.0001	26	51.02	0.0012 ± 0.0001	40	51.14	0.0011 ± 0.0000	54	55.24
	128	0.0013 ± 0.0000	41	200.07	0.0011 ± 0.0000	56	200.33	0.0012 ± 0.0000	81	200.58	0.0011 ± 0.0000	108	216.97
3	16	0.0018 ± 0.0003	7	4.06	0.0017 ± 0.0007	9	4.09	0.0015 ± 0.0004	12	3.85	0.0011 ± 0.0001	16	4.38
	32	0.0014 ± 0.0001	12	15.27	0.0013 ± 0.0003	16	15.34	0.0014 ± 0.0002	21	14.34	0.0011 ± 0.0000	29	16.42
	64	0.0013 ± 0.0000	22	59.21	0.0013 ± 0.0001	29	59.34	0.0012 ± 0.0001	40	55.30	0.0011 ± 0.0000	57	63.56
	128	0.0012 ± 0.0000	47	233.10	0.0011 ± 0.0001	62	233.35	0.0012 ± 0.0000	82	217.10	0.0011 ± 0.0001	113	249.99
4	16	0.0015 ± 0.0001	8	4.60	0.0022 ± 0.0013	10	4.63	0.0018 ± 0.0006	12	4.12	0.0011 ± 0.0001	16	4.92
	32	0.0013 ± 0.0000	13	17.38	0.0016 ± 0.0005	17	17.45	0.0012 ± 0.0001	21	15.40	0.0011 ± 0.0000	30	18.54
	64	0.0013 ± 0.0000	25	67.53	0.0012 ± 0.0001	32	67.66	0.0012 ± 0.0001	40	59.46	0.0011 ± 0.0000	59	71.88
	128	0.0012 ± 0.0000	52	266.12	0.0011 ± 0.0000	68	266.38	0.0012 ± 0.0001	82	233.61	0.0010 ± 0.0000	119	283.02